# Lumped Thermal Impedance Modeling of Anthropogenic Global Warming of the Troposphere

Geert Willems[*1], Wim Fyen[†1], Philippe Roussel[‡1], and Jan Van Houdt[§1,2]

[1]imec, Leuven, Belgium
[2]Department of Physics and Astronomy, KU Leuven, Belgium

This manuscript is a non-peer-reviewed preprint submitted to EarthArXiv. It is intended for subsequent submission to a peer-reviewed journal.

Version 1.0. EarthArXiv preprint. Submitted May 18, 2026

[*]Corresponding author: geert.willems@imec.be
[†]wim.fyen@imec.be
[‡]philippe.roussel@imec.be
[§]jan.vanhoudt@imec.be

**Abstract**

Anthropogenic global warming has reached a level so high that it is now possible to analyze its dynamics and spatial variation. Spatially varying Surface Air Temperature (SAT) anomalies [1] can be well described by exponential functions with increase rates that range from 2.1 to 3.7% per year, depending on the region. The Northern Hemisphere has warmed significantly more than the Southern Hemisphere and is also warming more rapidly. In this work, small-signal, lumped thermal impedance (LTI) modeling of the Earth thermal system is introduced as an efficient method to model the temporal and spatial variation of SAT across the globe at continental scale since the industrial revolution. SAT is, in first-order, determined by the warming of the troposphere as a consequence of energy sources dissipating heat in it. Due to its small thermal capacity, it has a high sensitivity to these sources. The thermal sensitivity of the troposphere is estimated to be $5.4\pm0.9$K per W/m$^2$ of dissipated energy. This value is derived from the troposphere's thermal response to the 11-year solar cycle. The spatially varied increase of 2.1 to 3.7% per year of SAT-anomaly cannot be simply explained by global uniform warming by uniformly distributed greenhouse gases (GHGs), dominated by $CO_2$, of which the concentration increases at a rate of only 1.9% per year. Within the framework of a small-signal LTI-model for the troposphere volumes above the Northern and Southern Hemisphere's oceans and land masses, respectively, three effective small-signal anthropogenic troposphere heat sources are identified and quantified consistent with the observed region-dependent exponential increase in SAT. These are: (i) IRTA: Infrared Radiation Absorption in the Troposphere determined by GHG-emission and quantified from the Southern Hemisphere ocean SAT-evolution; (ii) AHR: Anthropogenic Heat Release which directly heats the troposphere, independently derived from global primary energy consumption data; (iii) SITA: Solar Irradiation Absorption in the Troposphere increasing rapidly ($> 3\%$ per year) attributed to increasing levels of short-lived Anthropogenic Chemicals Emission (ACE). This heat source is quantified by fitting the impedance model equations to the continental SAT-evolutions since 1990. It amounts to an increase of close to $+0.2\%$ in solar irradiation absorption over the Northern Hemisphere's land. The global average increase in SITA coincides with the increase in OH-anomaly since 1990, consistent with the hypothesized chemical origin of SITA-warming [2]. The presented LTI-model quantifies the accelerating and spatially varying global warming as a result of exponentially increasing anthropogenic heat sources (IRTA, AHR, SITA) that cause a region-dependent exponentially increasing SAT since the industrial revolution. The results are derived within a small-signal, lumped linear thermal impedance framework and are bounded by the LTI-model structure, its linearization, and the estimations of the effective impedance parameters derived from SAT and Total Solar Irradiation measurements.

# 1 Surface Air Temperature variation

## 1.1 Spatial and temporal variation of global warming

Greenhouse gases (GHGs), especially $CO_2$, which are globally well-distributed, are considered to be the dominant agents causing global warming [3]. Nevertheless, there are large differences in warming between different continents, from as little as 0.3K in Antarctica to close to 3K in the Arctic [1]. SAT in Europe and, in general, over land in the Northern Hemisphere, is increasing twice as fast as the global average [1, 4]. Variations in GHG-concentrations do not explain spatial variations in anthropogenic warming. Changing weather patterns, reduced air-pollution, and the Northern location do not provide a convincing explanation for the observed heating rates of the Northern Hemisphere's land masses.

Anthropogenic global warming has become so pronounced that it is now possible to examine not only its magnitude but also its temporal and spatial variation with significant statistical confidence. Figure 1 shows the Surface Air Temperature (SAT) anomalies [1] and the Sea Surface Temperature anomalies (SST) [5] globally and in both hemispheres, as well as the SAT-anomalies over land and over the ocean, respectively. The reference temperature is the pre-industrial Global SAT (GSAT) for which the SAT-anomaly $\Delta GSAT(1750) = 0$. Consistent with the exponentially increasing anthropogenic heat sources driving global warming, see section 2, all SAT and SST-anomalies can be well described with an exponential function per Equation (1)

$$\Delta SXT(t) = \Delta SXT(t_0) a^{\frac{t-t_0}{t_r}} \tag{1}$$

with $t_r = 1$ year and X=A for SAT or X=S for SST, respectively.

The fitting of the warming trend data is affected by a temperature oscillation peaking around 1940 with a period of about 66 years. This oscillation may be related to a periodic Total Solar Irradiance (TSI) variation, see section 2.1, and may result in an overestimation of the fitted base $a$ of the exponential function. For that reason, the 1850-2025 full-range model fit was compared to a fit to the data from 1965 to 2025 only. The fit with the smallest base $a$ is considered to represent the warming trend in the best possible way and is selected for the warming trend models shown in Figure 1. For an exponentially increasing temperature anomaly (1) the instantaneous warming rate $\delta SXT(t)$ also increases exponentially, according to

$$\delta SXT(t) = \frac{\partial \Delta SXT(t)}{\partial t} = \ln a \cdot \Delta SXT(t_0) a^{\frac{t-t_0}{t_r}} \tag{2}$$

The uncertainties given in Figure 1 correspond to $2\sigma$ with $\sigma$ the standard deviations obtained from the covariance matrix of the nonlinear least squares fits.

The spatial differences between the magnitude and the rate of warming represented by the exponent base $a$, give essential clues to identify the heat sources that cause global warming. The distribution of the heat sources in the Earth thermal system, as well as the dynamics of their heat release and related heat transport throughout the Earth thermal system, provide crucial elements in the assessment of the impact of their individual contributions. This study applies a phenomenological, small-signal Lumped Thermal Impedance (LTI) framework to model the spatially varying warming dynamics to identify and quantify the effective heating agents contributing to the global SAT-increase and to quantitatively model the spatially varying SAT-anomaly at decadal and centennial scale since the industrial revolution. It does not provide direct mechanistic proof of underlying processes. Its results depend and are bounded by the LTI-model structure, its small-signal linearization, and the estimations of the effective impedance parameters derived from the selected SAT and Total Solar Irradiation measurements.

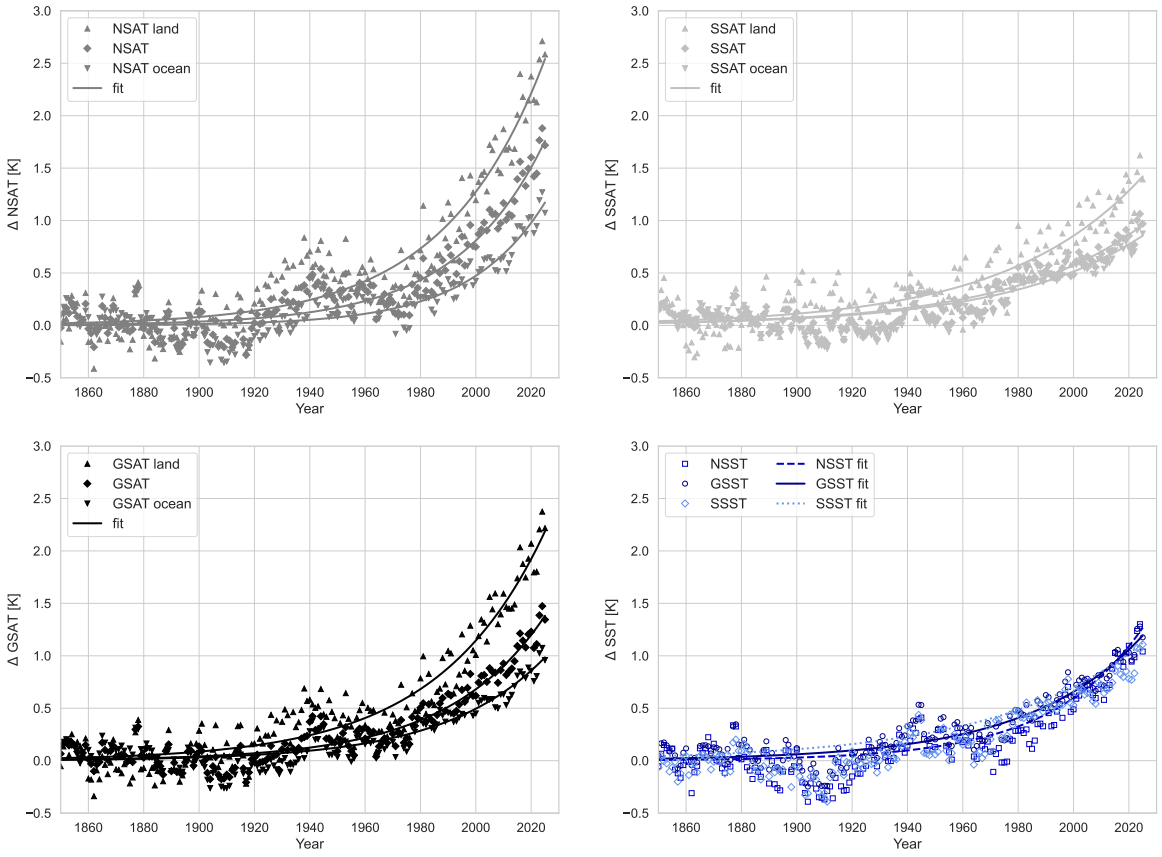


| | $\Delta T(2025) \pm 2\sigma$ [K] | 95% CI [K] | $\Delta a \pm 2\sigma$ [%/y] | 95% CI [%/y] | $\delta$SAT(2025) [K/dec] |
|---|---|---|---|---|---|
| GSAT | $1.38 \pm 0.07$ | 1.32–1.46 | $2.9 \pm 0.3$ | 2.5–3.2 | $0.39 \pm 0.05$ |
| $\text{GSAT}_{\text{land}}$ | $2.2 \pm 0.1$ | 2.1–2.3 | $2.6 \pm 0.3$ | 2.3–2.9 | $0.57 \pm 0.07$ |
| $\text{GSAT}^{*}_{\text{ocean}}$ | $0.99 \pm 0.06$ | 0.93–1.04 | $2.8 \pm 0.3$ | 2.5–3.1 | $0.27 \pm 0.03$ |
| NSAT | $1.8 \pm 0.1$ | 1.7–1.9 | $3.2 \pm 0.4$ | 2.8–3.5 | $0.55 \pm 0.07$ |
| $\mathbf{NSAT_{land}}$ | $\mathbf{2.5 \pm 0.1}$ | **2.4–2.7** | $2.8 \pm 0.4$ | 2.4–3.2 | $0.7 \pm 0.1$ |
| $\text{NSAT}_{\text{ocean}}$ | $1.2 \pm 0.1$ | 1.1–1.3 | $3.7 \pm 0.7$ | 3.1–4.3 | $0.43 \pm 0.08$ |
| SSAT* | $0.96 \pm 0.06$ | 0.90–1.02 | $2.1 \pm 0.3$ | 1.8–2.4 | $0.20 \pm 0.03$ |
| $\text{SSAT}^{*}_{\text{land}}$ | $1.4 \pm 0.1$ | 1.3–1.5 | $2.1 \pm 0.3$ | 1.7–2.4 | $0.29 \pm 0.05$ |
| $\text{SSAT}^{*}_{\text{ocean}}$ | $0.86 \pm 0.06$ | 0.80–0.91 | $2.1 \pm 0.3$ | 1.8–2.3 | $0.17 \pm 0.03$ |
| GSST | $1.21 \pm 0.08$ | 1.13–1.29 | $2.4 \pm 0.4$ | 2.1–2.8 | $0.29 \pm 0.05$ |
| NSST | $1.3 \pm 0.1$ | 1.2–1.4 | $3.1 \pm 0.5$ | 2.6–3.6 | $0.40 \pm 0.07$ |
| SSST* | $1.13 \pm 0.07$ | 1.07–1.20 | $1.9 \pm 0.2$ | 1.6–2.1 | $0.21 \pm 0.05$ |

Figure 1: Land, ocean, and average SAT and SST anomalies globally (G) and in the Northern (N) and Southern (S) hemispheres, fitted with exponential trend lines. Table columns: SAT or SST anomaly in 2025 ($\Delta T(2025)$); annual growth rate ($\Delta a$, where $a = 1 + \Delta a$) with its 95% confidence interval (CI) and $\pm 2\sigma$ uncertainty; and instantaneous warming rate $\delta$SAT(2025) in K/decade. **Bold** indicates the highest SAT-value. Gray-shaded cells indicate the highest SAT growth rate. *Fits based on 1965–2024 data.

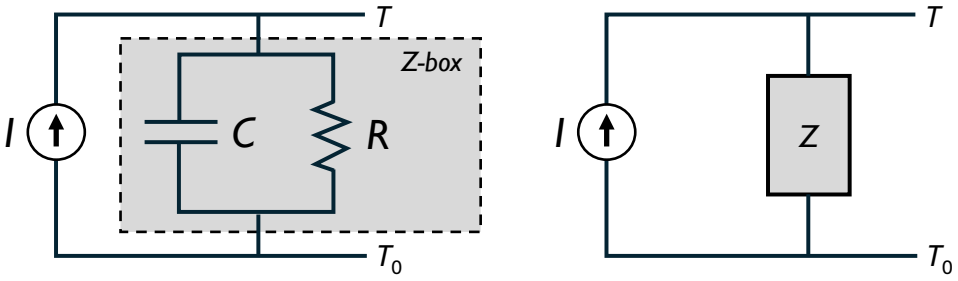


Figure 2: Left: Basic equivalent circuit of a thermal capacitor $C$ [J/K] loaded by a heat source $I$ [W] and losing its energy to a mass at a fixed temperature $T_0$ through a thermal resistor $R$ [K/W]. Right: the corresponding Z-box with single impedance $Z$.

### 1.2 Warming by exponentially increasing heat sources

The basic building block of a thermal impedance model for a Volume-of-Interest (VoI) of the Earth thermal system is shown in Figure 2. It consists of a heat source $I(t)$ charging a thermal capacitor $C$ representing the thermal capacity of the VoI and a parallel resistor $R$ through which the capacitor $C$ loses its energy $E = C(T - T_0) = C\Delta T$ to a mass at constant temperature $T_0$. The equation determining the temperature of the capacitor is

$$C\frac{\partial \Delta T}{\partial t} = I(t) - \frac{\Delta T}{R} \tag{3}$$

In the case of zero heat flux before time $t = t_0$ ($I(t < t_0) = 0$) and a constant heat flux $I(t \geq t_0) = I$ applied to the capacitor at time $t = t_0$, the temperature varies as

$$\Delta T(t) = RI(t_0)\left[1 - \exp\left(-\frac{t - t_0}{RC}\right)\right] \tag{4}$$

The stationary temperature $\Delta T(\infty) = RI$ is determined by the thermal resistance $R$ and the heat flux $I$. This asymptotic value is reached within 5% after a time $t \approx 3\tau$ or 1% within $t \approx 5\tau$, with $\tau = RC$ the relaxation time of the RC-system. The thermal capacitance $C$ determines the initial rate of temperature change

$$\left.\frac{\partial \Delta T}{\partial t}\right|_{t=t_0} = \frac{I}{C} \tag{5}$$

For an exponential heat source, $I(t) = I(t_0)a^{(t-t_0)}$, the solution of (3) yields

$$\begin{aligned} \Delta T(t) =& \frac{RI(t_0)a^{(t-t_0)/t_\mathrm{r}}}{1 + \frac{RC}{t}\ln a} + \left[\Delta T(t_0) - \frac{RI(t_0)}{1 + \frac{RC}{t_\mathrm{r}}\ln a}\right]\exp\left(-\frac{t - t_0}{RC}\right) \\ \approx& \frac{RI(t_0)a^{(t-t_0)/t_\mathrm{r}}}{1 + \frac{RC}{t_\mathrm{r}}\ln a} = RI(t_0)a^{(t-t_0-\Delta t_\mathrm{RC})} \text{ for large } t \end{aligned} \tag{6}$$

with $\Delta t_\mathrm{RC} = \log_a(\frac{RC}{t_\mathrm{r}}\ln a + 1)$. Equation (6) shows that an exponentially increasing heat source with base $a$ will result in an exponentially increasing temperature with the same base $a$, delayed by $\Delta t_\mathrm{RC}$. This can be generalized: the temperature of a VoI will follow its heat source with a delay determined by the thermal relaxation time constant $\tau = RC$ of the VoI. Additionally, the temperature increase rate cannot be higher than the increase rate of the heat source when $R$ and $C$ are approximately temperature independent. Consequently, an exponentially increasing SAT with exponential base $a$ implies that it is driven by one or more exponentially increasing heat sources that match the SAT-increase rate determined by base $a$.

The observed acceleration of global warming [6] is a straightforward consequence of global warming being driven by exponentially increasing anthropogenic heat sources. The global warming rate $\delta GSAT(2025) = 0.39 \pm 0.05$K per decade in 2025, see Figure 1, is consistent with the work of Foster and Rahmstorf [6].

### 1.3 Thermal capacity of the troposphere

Today's global warming amounts to an increase in GSAT close to 1.5K or about 0.5% of $GSAT = 288.15\text{K}$ [7]. Such a small SAT-variation may arise from relatively small heat sources emitted in a volume with a small thermal capacitance and sufficient resistance to heat loss. AHR, directly dissipated in the troposphere is such a case.

The troposphere holds about 80% of the total mass of the atmosphere [3]. Its equivalent effective thermal capacitance $c_\text{t}$ expressed per unit of area can be derived from its total thermal energy content $e_\text{t}$ per unit of area and $GSAT$ as $c_\text{t} = e_\text{t}/GSAT$ with

$$e_\text{t} = \int_0^{h_\text{t}} c_\text{p}\rho(h)T(h)dh \tag{7}$$

$c_\text{p}$ being the isobaric specific heat of air, $h$ the height, $h_\text{t} = 11\text{km}$ the standard height of the tropopause and $T(h) = GSAT - Lh$ the temperature as a function of height with lapse rate $L = 6.5\text{K/km}$ [7]. The air density as a function of height can be derived from the barometric formula and the ideal gas law

$$\begin{aligned} \rho(h) &= \rho(0)\left(1 - \frac{Lh}{GSAT}\right)^{\frac{Mg}{RL}-1} \\ \rho(0) &= \frac{P_0 M}{R \cdot GSAT} \end{aligned} \tag{8}$$

with $R$ the ideal gas constant, $M$ the mean molar mass of air, $P_0$ the air pressure at sea level, and $g$ the gravitational acceleration. Calculating the integral of Equation (7) yields an effective thermal capacitance per unit area for the troposphere of

$$c_\text{t} = \frac{e_\text{t}}{GSAT} = 7.3\text{MJ/Km}^2. \tag{9}$$

consistent with the previously published value for the atmosphere of $c_\text{a} = 10.2\text{MJ/km}^2$ [8].

## 2 Troposphere warming agents

### 2.1 Total Solar Irradiance and its variation

The troposphere is heated by several heat sources, of which direct heating by the absorption of solar radiation is the dominant one. According to the Earth's energy budget [3] the fraction of TSI absorbed in the atmosphere amounts to $i_\text{a} = 80\text{W/m}^2$ of which about 80% or $i_\text{t} = 64\text{W/m}^2$ is absorbed in the troposphere [3]. TSI is not constant. The 11-year solar cycle results in a periodic variation of troposphere temperature [9]. However, this is not the only periodic variation of TSI. Figure 3 shows the frequency spectrum of the 1959-2004 GSAT and TSI variation data used by Camp and Tung [9] for the analysis of the SAT-response to the 11-year solar cycle. It reveals TSI-peaks with corresponding temperature peaks not only at the 11-year period but also at 66, 22 and 16.5 years, i.e., at respectively 1, 3, and 4 times the 66-year cycle frequency, respectively. The 66-year cycle may be a harmonic of even longer periodic variations. Several other peaks in the $\mathcal{F}(GSAT, i\omega)$ and $\mathcal{F}(TSI, i\omega)$ spectra occur near the higher frequency harmonics of the 66-year TSI cycle. Note that the 66-year period is twice the period of the 33-year Brückner-Egeson-Lockyer climate cycle [10] while the El Niño Southern Oscillation (ENSO) periods match the higher frequency harmonics.

These TSI-variations obscure the warming trend of anthropogenic heat sources. The 66-year cycle may be the cause of the increase of SAT and SST between 1930-1950, see Figure 1. A quantitative modeling of these variations and their SAT-impact would allow one to filter out these natural small TSI-induced SAT-variations from the temperature anomaly measurement, allowing for further improvement of the quantification of anthropogenic climate effects.

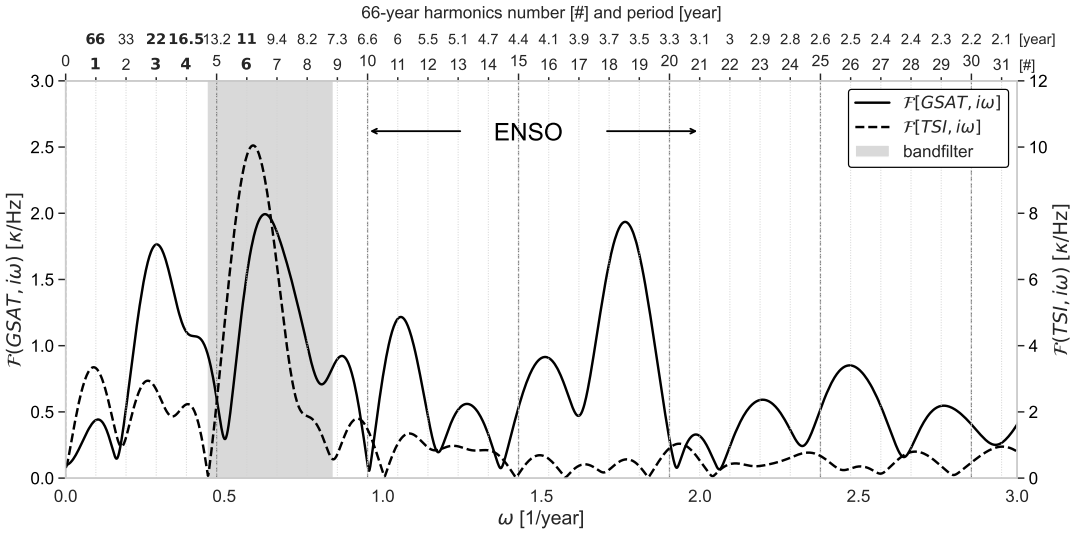


Figure 3: Frequency spectrum of 1959-2004 GSAT and TSI measurements [9] revealing the periodicity in SAT-variation correlating with the harmonics ($\#=3,4,6$) of a 66-year solar cycle ($\#=1$). Grey zone: band-pass filter position used in troposphere impedance determination.

The 100m thick well-mixed ocean surface layer has a thermal capacity which is an order of magnitude larger than that of the troposphere. Therefore, the impact of the 11-year solar cycle on its temperature is significantly dampened [11]. This is not the case for longer period TSI-cycles. The ocean surface absorbs twice as much solar irradiation as the troposphere itself [3]. Therefore, the impact of small, long-period TSI-variations ($\#<6$) on SAT may be significant through indirect heating of the surface air by the warming ocean surface, even with a TSI-variation amplitude that is less than that of the pronounced 11-year TSI-variation.

## 2.2 IRTA: Troposphere warming by Infrared Radiation Absorption

The troposphere also absorbs terrestrial and stratospheric infrared (IR) radiation and loses heat through IR-radiation to space. GHGs reduce this loss and may increase the absorption of IR-radiation. A disturbance in the IR-radiation balance forms a net small-signal troposphere heat source, which we will call Infrared Radiation Troposphere Absorption (IRTA). The increase in anthropogenic IRTA since the industrial revolution is dominated by the emission of $CO_2$. The increase in $CO_2$-concentration in the atmosphere since 1750 shown in Figure 4 [12, 13], can be well described by an exponential function:

$$[CO_2(t)] = [CO_2(1750)] + [\Delta CO_2(t_0)]a^{(t-t_0)/t_r}\ [\text{ppm}] \tag{10}$$

$$\begin{aligned} a &= 1.0188 \pm 0.0004 \\ [\Delta CO_2(2025)] &= 146 \pm 2\text{ppm} \\ [CO_2(1750)] &= 278\text{ppm} \end{aligned} \tag{11}$$

with $t_0 = 2025$, $t_r = 1$ year, $[CO_2(1750)]$ pre-industrial $CO_2$-concentration, and $[\Delta CO_2(2025)]$ increase in $CO_2$-concentration in 2025 compared to $[CO_2(1750)]$. The uncertainty is specified by $\pm 2\sigma$ with $\sigma$ the standard deviation of the fit. The common understanding is that $F_{CO_2}$, the radiative GHG-forcing by $CO_2$, depends logarithmically on the $CO_2$-concentration according to the simplified expression [14]

$$\Delta F_{CO_2} = 5.35 \ln \frac{[CO_2](t-t_0)}{[CO_2](t_0)}\ [\text{W/m}^2] \tag{12}$$

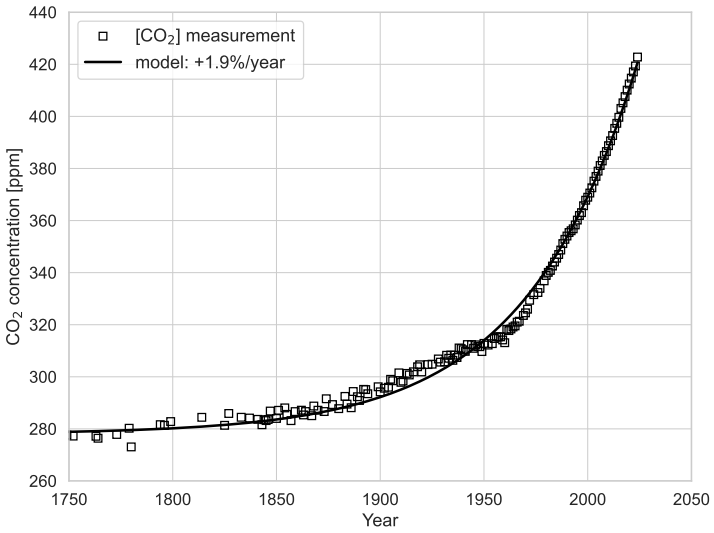


Figure 4: $CO_2$-concentration [12] with an exponential growth model of 1.88% per year.

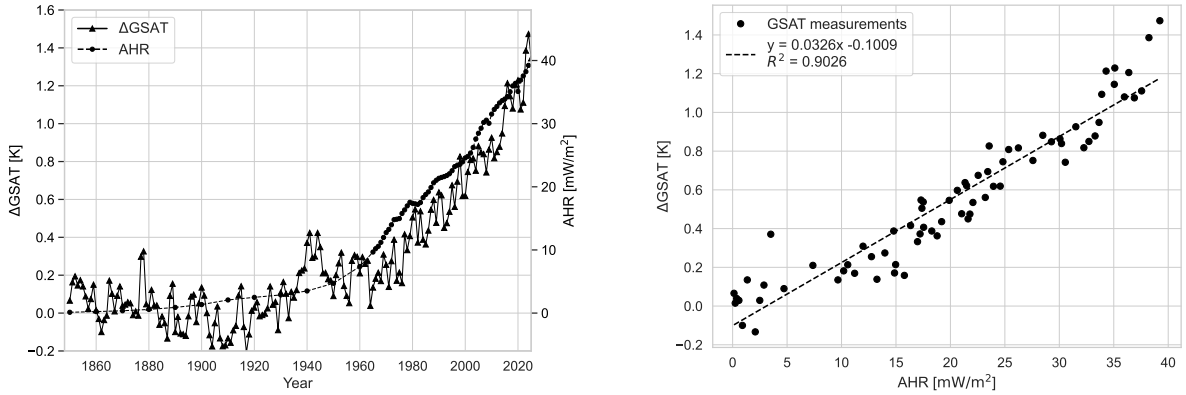


(a) Evolution of $AHR$ and $\Delta GSAT$ since 1880.

(b) Correlation between $\Delta GSAT$ and $AHR$

Figure 5: Comparison of GSAT-anomaly $\Delta GSAT$ [16] and primary energy consumption as AHR proxy [17].

or

$$F_{CO_2}(t) = 5.35 \left[ 1 + \ln \left( 1 + \frac{[\Delta CO_2](t_0) \cdot a^{(t-t_0)/t_r}}{[CO_2](t_0)} \right) \right] \ [W/m^2] \tag{13}$$

which increases more slowly than the 1.88% per year increase in $CO_2$-concentration.

The $CO_2$-increase rate and thus the related IRTA-increase rate are significantly lower than the observed average SAT-increase rates of 2.9% per year globally and of 3.2% per year in the Northern Hemisphere, see Figure 1. The SAT-increase rate in the Southern Hemisphere of 2.1% per year lies closer to but still above the $CO_2$-increase rate. Additionally, atmospheric concentrations of methane, nitrous oxide, and other GHGs do not increase at a sufficiently high rate to explain the observed, location-dependent, rapid SAT-increase [3, 15] within the LTI-model framework.

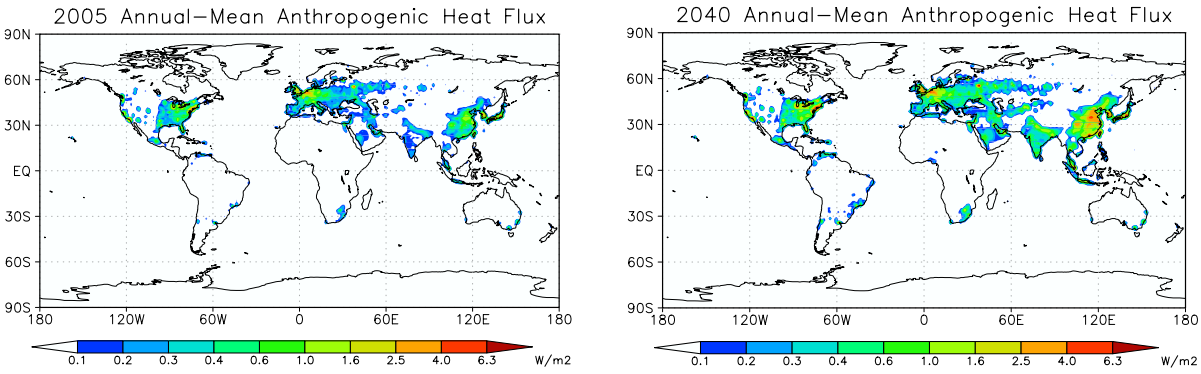


Figure 6: Estimated and projected AHR world distribution showing the high levels of AHR in Europe, the North American east coast and China [18].

## 2.3 AHR: Troposphere warming by Anthropogenic Heat Release

### 2.3.1 Relevance of Anthropogenic Heat Release for global warming

Humanity's primary energy consumption directly warms the troposphere, since according to the second law of thermodynamics, it turns into heat that is predominantly released into the troposphere. Primary energy consumption makes up the largest part of Anthropogenic Heat Release (AHR) [18]. It gives a lower limit to AHR since certain AHR-contributions are not included: waste heat from renewable electricity generation [19], heat from various types of waste burning, human-caused fires, etc. For simplicity, we will use primary energy consumption as a proxy for AHR.

Figure 5 shows the AHR [17] and GSAT-anomaly time series [16], and their strong correlation. This corroborates the anthropogenic origin of global warming, since AHR is a proxy for human activity in general, but it does not imply that AHR is the (sole) cause of global warming. AHR, $CO_2$, and other anthropogenic emissions are strongly interlinked, since fossil fuels are still the main source of energy (87% in 2024 [19]) and thus the main source of AHR and the emission of anthropogenic $CO_2$. This poses a challenge to unravel the impact of the different heating agents.

The correlation between the spatial variations of the SAT-anomaly and the AHR-distribution provides a means to accomplish this disentanglement. Figure 6 shows the global distribution of AHR [18] with high AHR-levels in Europe, especially in the Benelux-Rhine-Ruhr region, the North-American East coast and China. This correlates well with the significantly higher SAT-anomaly over land in the Northern Hemisphere, see Figure 1, and the rapid warming of Europe. The primary energy dissipation density of $223\mathrm{mW/m^2}$ (2024) in Europe is six times higher than the global average of $37\mathrm{mW/m^2}$ [19]. To put this into perspective, Europe's energy dissipation density is comparable to the effective radiative forcing (ERF) attributed to methane ($CH_4$: $ERF = 276\mathrm{mW/m^2}$ [3]).

### 2.3.2 AHR modeling

Since 2012, approximately 93% of global AHR has been released in the Northern Hemisphere. Between 1965 and 2012, primary energy consumption in the Southern Hemisphere increased from 4% to 7% of total energy consumption. The average AHR dissipated globally ($X = G$), in the Northern ($X = N$), and in the Southern ($X = S$) Hemispheres, can be characterized by approximately constant yearly growth rates $\Delta a_r\%$ per year and be described by exponential functions (14)

$$XAHR_r(t) = XAHR_r(t_0) \cdot a_r^{(t-t_0)/t_\mathrm{r}} \tag{14}$$

with base $a_r = 1 + \Delta a_r$, $t_\mathrm{r} = 1$ year, and $r$ indicating the average AHR-dissipation over the to-be-specified subregion. The base $a_r$ is obtained by fitting to the primary energy consumption

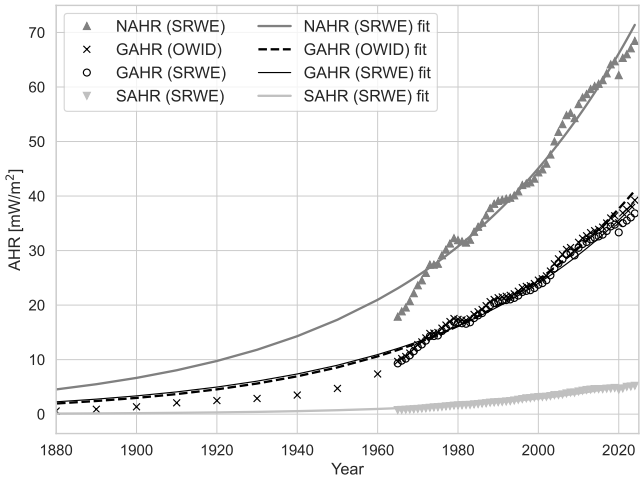


| [EJ/y] | $AHR(2025) \pm 2\sigma$ | 95% CI |
|---|---|---|
| GAHR* | $670 \pm 10$ | 660 - 690 |
| GAHR | $630 \pm 10$ | 620 - 640 |
| NAHR | $590 \pm 10$ | 580 - 600 |
| SAHR | $47 \pm 2$ | 45 - 48 |
| [mW/m$^2$] | $AHR(2025) \pm 2\sigma$ | 95% CI |
| GAHR* | $41.9 \pm 0.9$ | 41.0 - 42.8 |
| GAHR | $39.3 \pm 0.7$ | 38.5 - 40.0 |
| $\text{GAHR}_{\text{land}}$ | $135 \pm 3$ | 133 - 138 |
| NAHR | $73 \pm 1$ | 71 - 74 |
| $\text{NAHR}_{\text{land}}$ | $187 \pm 4$ | 183 - 190 |
| SAHR | $5.8 \pm 0.2$ | 5.6 - 6.0 |
| $\text{SAHR}_{\text{land}}$ | $31 \pm 1$ | 30 - 32 |
| [%/y] | $\Delta a \pm 2\sigma$ | 95% CI |
| GAHR* | $2.14 \pm 0.09$ | 2.05 - 2.22 |
| GAHR | $1.99 \pm 0.08$ | 1.91 - 2.06 |
| NAHR | $1.93 \pm 0.08$ | 1.86 - 2.01 |
| SAHR | $2.8 \pm 0.2$ | 2.7 - 3.0 |

Figure 7: Average AHR in the Northern Hemisphere ($NAHR$), Southern Hemisphere ($SAHR$), and globally ($GAHR$) fitted with exponential growth models per Eq. (14). Table lists parameters including AHR levels over land. Accuracy indicated by the 95% confidence interval (CI) and $2\sigma$ with $\sigma$ the standard deviation, both obtained from the covariance matrix of the least-squares fit. OWID(*): data of Our World in Data; SRWE: Energy Institute data.

data published in the Statistical Review of World Energy 2025 report (SRWE) [19] of the Energy Institute and of Our World in Data (OWID) [17] for comparison, see Figure 7. AHR is generated almost entirely on land. Therefore, the average AHR-densities over land can be obtained from the global fit results and the fit results for both hemispheres, by dividing the respective AHR-values by the corresponding land area fraction. This yields ($NAHR_{\text{land}} = 187\text{mW/m}^2$) on land in the Northern Hemisphere, which is comparable to Europe's AHR ($EUAHR = 223\text{mW/m}^2$). The average AHR in the Southern Hemisphere ($SAHR = 5.81\text{mW/m}^2$) is rapidly increasing at 2.8% per year but is still far below the global average.

The GAHR-increase rate of about 2% per year is only slightly higher than the annual [$CO_2$]-increase rate of 1.88% per year. This is consistent with the fact that AHR predominantly originates from the burning of fossil fuels [19]. Comparing the temperature anomalies of Figure 1 with Figure 7 reveals that the largest SAT-anomalies are measured where AHR is the most intense. These Figures show that the SAT-increase rates are equal to or larger than those of AHR.

### 2.3.3 AHR versus Effective Radiative Forcing

AHR is a controversial topic [20–27]. A General Circulation Model (GCM) study by Flanner [18] predicts a continental-scale warming of 0.44K for the USA, 0.54K for Europe, to 0.88K for East Asia by 2100 due to AHR. Chen et al. [24] state that: "AHR is a tiny but essential factor in global climate and long-term climate change that should not be ignored". The position of the IPCC since its fourth assessment report AR4 (2007) [28] is that AHR can cause local warming in cities but is negligible on a global scale. This is based on the observation that the global average AHR is three orders of magnitude smaller than the TSI absorbed by Earth and its infrared (IR) emission, both in the order of several 100W/m$^2$. The AHR is also only slightly larger than 1% of the top-of-the-atmosphere, total effective anthropogenic radiative forcing (ERF) of 2.84W/m$^2$ [3]. However, system theory learns that the impact of a small input signal on the output of a system cannot be assumed negligible, merely because its magnitude is significantly smaller than other inputs. For any system, the output depends on how the different inputs interact with the internal structure of the system and its dynamics. In 2024, global primary energy consumption

$E = 592$EJ [19] is sufficient to heat the troposphere by

$$\Delta T = \frac{E}{c_t A} = \frac{592\ 10^{18}\ \text{J}}{3700\ 10^{18}\ \text{J/K}} = 0.16\text{K} \tag{15}$$

with $c_t = 7.3\text{MJ/Km}^2$ and $A = 5.1 \cdot 10^{14}\text{m}^2$ being the Earth's surface area. This is equal to about 10% of today's total GSAT-anomaly. Whether or not this amount of heat is negligible depends on how fast the troposphere can lose its absorbed energy $E$ to its surroundings, i.e., on the value of the thermal resistance $R$ of the troposphere's Z-box model, see Figure 2.

AHR is mainly dissipated in the low thermal capacitance of the troposphere, whereas a large fraction of the radiative forcing fluxes to which AHR is being compared are absorbed or emitted by the much larger thermal capacitance of the ocean and deep Earth, of which the temperature does not change significantly in the short-term ($t \ll \tau = RC$). The location of heat dissipation is of critical importance for its impact on the temperature distribution in the Earth thermal system. An AHR impact study requires a method that properly addresses dynamic heat flow between different parts of the atmosphere, and between the atmosphere, the oceans, land, and space. GCMs can accomplish this task. However, few GCM-studies of global warming include AHR [18, 24, 29–31].

### 2.4 SITA: Troposphere warming by increased Solar Irradiation Absorption

An additional anthropogenic heat source for the troposphere is a change in the fraction of incoming solar irradiation absorbed within it. We will use the term Solar Irradiation Troposphere Absorption (SITA) to denote the change in solar energy absorbed in the troposphere relative to a pre-industrial reference state and attribute it to the collective presence of a broad set of mostly short-lived airborne chemicals released by human activities called Anthropogenic Chemical Emission (ACE). All constituents of the atmosphere absorb electromagnetic radiation at specific wavelengths. Studies show that certain Volatile Organic Compounds (VOCs) can have a measurable effect on the optical properties of the atmosphere throughout the solar spectrum at low concentrations [32]. More generally, an increase in the concentration and diversity of anthropogenic airborne molecules is expected to alter atmospheric radiative absorption characteristics. This change predominantly redistributes solar energy absorption vertically in the Earth thermal system, increasing the absorbed solar energy in the troposphere while correspondingly reducing the fraction reaching the surface. As a result, this effect is expected to be weakly expressed in top-of-the-atmosphere energy balance metrics and may not be captured by standard radiative forcing diagnostics. In this framework, SITA encompasses the direct solar absorption and scattering effects of Short-Lived Climate Forcers (SLCFs) [33] such as aerosols, as well as the potential solar spectrum absorption effects of species whose climate influence is traditionally assessed only through their contribution to infrared radiative forcing, e.g., some halogenated compounds, or through their indirect role as a precursor for direct SLCFs such as Non-Methane Volatile Organic Compounds (NMVOCs). We explicitly distinguish SITA from infrared radiative effects captured by IRTA, even though both phenomena arise from changes in atmospheric composition caused by anthropogenic emission of chemicals.

For low atmospheric concentrations, the absorption length of ACE species is expected to exceed the troposphere height. In this regime, the Beer-Lambert law implies that the absorption coefficient and associated heating will increase approximately proportionally to the concentration. Although the contribution of any single compound is expected to be small, the aggregated radiation absorption effect of a large set of airborne chemicals with optical characteristics spanning broad wavelength ranges may become significant. The current absorption of solar energy in the atmosphere of $80\text{W/m}^2$ can be used as a reference [3]. An increase of only 0.1% in this absorption amounts to $64\text{mW/m}^2$ (80% of the atmosphere mass) heat dissipation in the troposphere. This is already 60% higher than the global average AHR in 2025. Given the fact

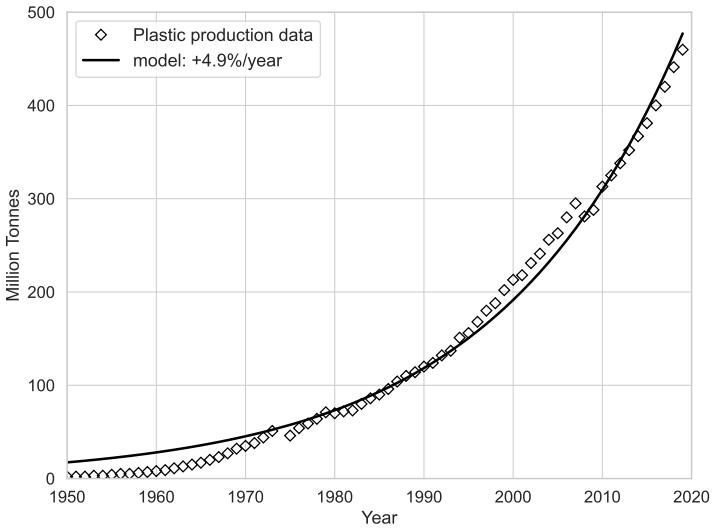


Figure 8: Plastic production [34] with an exponential growth model of 4.9% per year.

that this contribution can be of the same order as AHR we introduce increasing SITA caused by exponentially increasing ACE (SITA/ACE) as a working hypothesis to explain the observed accelerating global warming in the last four decades. We provide observations that support this hypothesis. Further proof may be obtained from the quantification of the region-dependent concentration of airborne anthropogenic chemicals and their optical properties.

For the SITA/ACE-hypothesis to be valid, there must be evidence that ACE is increasing at a rate that significantly exceeds the pre-1990 GSAT growth rate of about 2% per year. Quantitative information on the atmospheric burden and optical properties of the full spectrum of ACE species is still limited [33]. However, emissions of several classes of anthropogenic chemicals have increased rapidly in recent decades. Global plastic production, which can be associated with the emission of polymer precursors, solvents, additives, among others, has grown exponentially since the mid-20th century, with an average growth rate of 4.9% per year [34], see Figure 8. Many other industrial [35] and agricultural activities, as well as chemistry applications [36] lead to a rapid increase in ACE. Inventories of industrial NMVOC-emissions exhibit sustained multi-decadal growth in several heavily industrialized regions. Qiu et al. [37], show that the total industrial emission of NMVOC in China has increased by a factor of 11.6 between 1980 and 2010 or approximately 8.5% per year. The study of Li et al. [38] confirms the persistent increase in NMVOCs emission in China with an estimated tripling between 1990 and 2017 or a growth rate of more than 4% per year. The production and use of chemicals is much higher in the Northern Hemisphere than in the Southern Hemisphere. This may explain the much higher SITA/ACE-warming in the Northern Hemisphere because short-lived ACE, like all SLCF, are concentrated near their emission location, as opposed to well-mixed GHG [33]. All these observations are consistent with the SITA/ACE-hypothesis. However, they do not prove causality between ACE and SITA.

The SITA/ACE-hypothesis and the acknowledgment of AHR as a global warming agent do not seek to replace radiative forcing frameworks, but to complement them by highlighting these dynamical heat flow pathways that warrant quantitative examination within the troposphere's warming dynamics and which may be underrepresented in equilibrium oriented formulations and GCM-based studies.

# 3 Lumped thermal impedance modeling

## 3.1 General Circulation Modeling of large-scale warming

GCMs are complex and require significant computational power. This makes them only accessible for specialized GCM-experts. To study warming effects on large scales, GCMs are also not very efficient. They integrate the GCM-results over the VoI to determine their average warming, discarding most of the painstakingly obtained details of the calculation. For that reason, we propose a Lumped Thermal Impedance (LTI) model which directly calculates the average temperature of a large scale VoI with the required heat transfer resolution in space and time, but not more than needed. This provides insight into the large-scale dynamics of the Earth thermal system's internal heat flows in an efficient and effective way. It can address localized, dynamic heat sources such as AHR without the need of a computational intense GCM. Furthermore, this complementary approach to GCM is expected to be more accessible to a broad research community.

## 3.2 Generic lumped thermal impedance model

Figure 9 shows one dimension of the basic building block of a generic LTI-model. The expansion into three dimensions is straightforward. To determine the average temperature $T(x_i, y_j, z_k)$ of a VoI $V(x_i, y_j, z_k)$, the thermal response of the VoI to energy sources $I^s_{i,j,k}$ and drains $O^d_{i,j,k}$ is modeled using a thermal capacitance $C(x_i, y_j, z_k)$ that is linked to the mass of the VoI. A set of thermal resistances $R_{u,v,w}$ carries the volume's heat exchange fluxes that depend linearly on the temperature differences with surrounding volumes. Thermal resistances typically represent conductive and convective heat transfer between parts of the Earth thermal system. Linearized radiative heat transfer can be included. Heat sources $I^s_{i,j,k}$ and drains $O^d_{i,j,k}$ describe heat transfer between volumes that may not be adjacent to each other or that do not depend linearly on the temperature difference between volumes exchanging energy. The heat sources can be external to the system, e.g., solar radiation absorption and IR-radiation to space, or internal to the system, e.g., IR-radiation exchanges between different parts of the Earth thermal system. The superscripts $s$ and $d$ identify the locations of the sources and drains, respectively.

The temperature of the $N$ volumes is found by solving the set of $N = N_x \times N_y \times N_z$ Equations (16) using the appropriate boundary conditions for the system

$$\begin{aligned} C(x_i, y_j, z_k)\frac{\partial T(x_i, y_j, z_k)}{\partial t} &= \sum_s I^s_{i,j,k} - \sum_d O^d_{i,j,k} \\ &+ \frac{T(x_{i-1}, y_j, z_k) - T(x_i, y_j, z_k)}{R(i^-, j, k)} + \frac{T(x_{i+1}, y_j, z_k) - T(x_i, y_j, z_k)}{R(i^+, j, k)} \\ &+ \frac{T(x_i, y_{j-1}, z_k) - T(x_i, y_j, z_k)}{R(i, j^-, k)} + \frac{T(x_i, y_{j+1}, z_k) - T(x_i, y_j, z_k)}{R(i, j^+, k)} \\ &+ \frac{T(x_i, y_j, z_{k-1}) - T(x_i, y_j, z_k)}{R(i, j, k^-)} + \frac{T(x_i, y_j, z_{k+1}) - T(x_i, y_j, z_k)}{R(i, j, k^+)} \end{aligned} \tag{16}$$

with $i = 1...N_x$, $j = 1...N_y$, and $k = 1...N_z$ running over the number $N$ of volumes in the system in the three spatial dimensions, and $s$ and $d$ over the number of sources and drains connected to volume $V(x_i, y_j, z_k)$.

For a lumped approach to deliver accurate results, volumes $V(x_i, y_j, z_k)$ need to be thermally in an internal quasi-static state, i.e., no significant internal temperature redistribution may occur on the timescale-of-interest ($t_{\min} \leq t \leq t_{\max}$). This requirement is typically fulfilled when the resolution $\Delta t$ of the timescale-of-interest is three to five times the relaxation time constant $\tau$ of the heat distribution within the volumes, depending on the required precision. This lumped approach can be used for any resolution scale: from the GCM cell-level, where it becomes

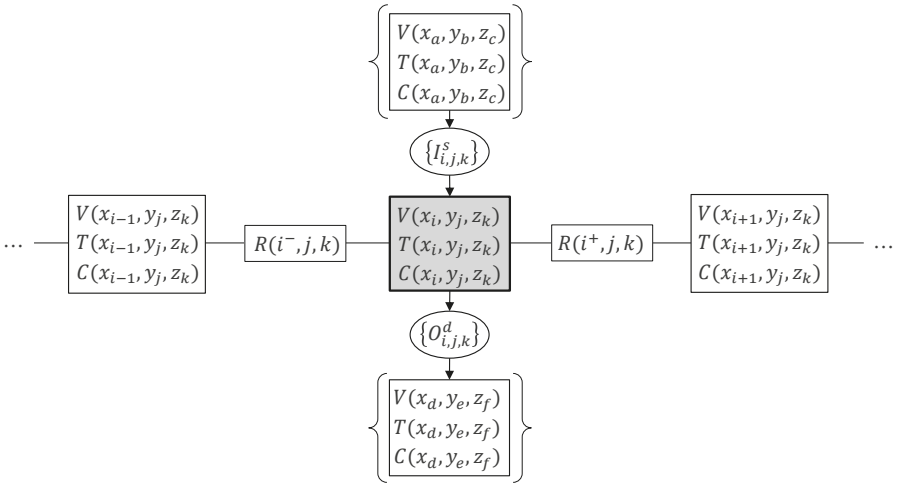


Figure 9: $x$-dimension of the basic building block of an LTI-model of a system consisting of volume $V(x_i, y_j, z_k)$ connected in the $x$-dimension with neighboring volumes $V(x_{i-1}, y_j, z_k)$ and $V(x_{i+1}, y_j, z_k)$ through thermal resistances $R_{i^-,j,k}$ and $R_{i^+,j,k}$, respectively, and exchanging energy through sources $I^s_{i,j,k}$ and drains $O^d_{i,j,k}$.

equivalent to GCM, to the single volume model of the energy balance framework with a single global surface temperature and a single thermal resistor related to the climate sensitivity [3].

The thermal capacitance can be estimated using the total mass of the VoI and the specific thermal capacity of its medium (air, water, soil, rock). The thermal capacitance per unit of area of the atmosphere ($c_\mathrm{a}$), of the ocean ($c_\mathrm{o}$), and of deep Earth ($c_\mathrm{r}$) differ in size by several orders of magnitude: $c_\mathrm{r} \approx 10^3 c_\mathrm{o} \approx 10^6 c_\mathrm{a}$. Hence, in first-order, their response rates to heat fluxes differ in magnitude by the same orders of magnitude. Therefore, to determine SAT one cannot model the Earth thermal system as a single thermal capacity and a single thermal resistance $R$ for any relevant timescale except a geological one.

Quantification of the thermal resistances connecting the thermal volumes is a prerequisite of the LTI-model. GCM could be used to calculate representative thermal resistances. In this paper a second approach is applied, i.e., the determination of the thermal resistance values based on the thermal response of certain volumes to known cyclic variable heat sources like variable solar irradiation absorption (diurnal, seasonal, 11-year solar cycle). The cycle-period must lie within the timescale-of-interest or be comparable to the relaxation time constant $\tau = RC$ related to the thermal resistance to be evaluated.

### 3.3 Simplification methodology

The presented LTI-approach uses linear response, small-signal approximation, fixed VoIs, and time-invariant parameters on the timescale-of-interest. The crux of using a lumped approach at the timescales-of-interest is the careful definition of the VoIs for which the heat transfer *within* the VoI can be considered as quasi-static, but not *between* the VoI and its surroundings. For such a case, the following two simplification methods can be applied to the set of Equations (16).

### 3.3.1 Relaxation-time-based simplification

If the relaxation time $\tau$ of a thermal volume is significantly *smaller* than the minimum timescale-of-interest $t_{\min}$, i.e., $\tau = RC < t_{\min}/(3 \text{ to } 5)$, the thermal capacitance of the volume can be neglected assuming $C \approx 0$, and the temperature of the volume approaches its stationary state for which $C\frac{\partial T}{\partial t} \approx 0$, see section 1.2. The temperature is only determined by the thermal resistances and the heat sources and drains.

If the relaxation time $\tau$ of a thermal volume is much *larger* than the maximum of the timescale-of-interest $t_{\max}$, i.e., $\tau = RC > (3 \text{ to } 5) \times t_{\max}$, the thermal capacitance of that volume can be approximated as $C \approx \infty$ implying a constant temperature of the volume.

### 3.3.2 Small-signal-based simplification

A second set of simplifications uses the fact that global warming is about an increase of the order of 1% of GSAT caused by energy fluxes of magnitudes in the range of 0.1% to 1% of energy fluxes (100-400W/m$^2$) [3] that create Earth's thermal equilibrium at $GSAT = 288.15$K [7]. This kind of problem can be treated using small-signal analysis, a well-known method of electronics engineering. This first-order perturbation calculation approach can be used to simplify and solve the set of Equations (16). The equations are linearized around a bias point, in this case the pre-industrial status of SAT and anthropogenic emissions ($t_0 = 1750$), using constant thermal capacitances $C(T_0)$ and resistances $R(T_0)$. It directly calculates the deviation $\Delta T = T - T_0$ from the bias point value $T_0$ resulting from small variations of the energy sources $\Delta I = I - I_0$ and drains $\Delta O = O - O_0$. Additionally, linearization enables the separate treatment of the different heat sources and to obtain the combined temperature impact by superposition.

## 3.4 Multi-Z-box model for the Earth thermal system

Figure 10 shows a thermal impedance scheme for the Earth thermal system that models heat exchanges over land and ocean, and between both. The scheme uses Z-boxes as defined in Figure 2, characterized by a thermal impedance $Z$ consisting of a resistor $R$ [W/K] in parallel with a capacitor $C$ [J/K]. The impedances $Z$ are defined in Table 1 together with the net heat sources $\Delta I$ [W] that release or drain heat into or from the Z-boxes. Thermal resistances $R$ connect certain Z-boxes for which a temperature difference may exist across an interface, e.g., the air-water interface. The scheme can be used for global analysis. It can be readily expanded by creating equivalent schemes for smaller areas. By adding Z-boxes for sea ice or land ice, ice-covered regions can be included. This expansion and the discussion of the modeling of all heat sources and impedances is beyond the scope of this paper.

We will focus on the troposphere using the basic scheme of Figure 2 and the troposphere thermal impedances $Z_{\text{land}}^{\text{trops}}$ and $Z_{\text{ocean}}^{\text{trops}}$ of Figure 10. The net heat release in the troposphere over the ocean $\Delta I_{\text{ocean}}^{\text{trops}}$, $\Delta I_{\text{ocean}}^{\text{tropp}}$ and over land $\Delta I_{\text{land}}^{\text{trops}}$, $\Delta I_{\text{land}}^{\text{tropp}}$, consists of:

- absorbed solar irradiation (SITA);
- net absorbed IR-radiation (IRTA) consisting of:
  - the absorption of IR-radiation emitted by Earth's surface;
  - the absorption of IR-radiation emitted by the stratosphere;
  - minus the IR-radiation emitted to space, which is predominantly part of the heat emitted near the tropopause, i.e., $\Delta I_{\text{ocean}}^{\text{tropp}}$ and $\Delta I_{\text{land}}^{\text{tropp}}$;
- direct energy dissipation (AHR).

Convective and conductive heat transfer between the troposphere and its surroundings, as well as latent heat release by condensation of evaporated water and heat lost by rainfall, are included in the region-dependent, effective thermal resistances $R_r^{\text{trops}}$ of the troposphere.

Table 1: Thermal impedances $Z = R//C$, interface resistors $R$, heat sources $\Delta I$, and temperature variations $\Delta T$ of the basic lumped impedance model of Figure 10. X indicates the modeled region, e.g., global, the hemisphere, continent, etc. The subscript indicates land or ocean.

| | |
|---|---|
| $Z^{\text{trops}}_{\text{land}}$, $Z^{\text{trops}}_{\text{ocean}}$ | The troposphere thermal impedance. |
| $Z^{\text{strats}}_{\text{land}}$, $Z^{\text{strats}}_{\text{ocean}}$ | The stratosphere thermal impedance. |
| $Z_{\text{hab}}$ | The thermal impedance of the inhabited layer of air in which AHR is released. |
| $Z_{\text{land}}$ | The thermal impedance of the land layer of a few meters thick that is affected by temperature variations of the air above it and by sunlight absorption. |
| $Z_{\text{Earth}}$ | Deep Earth thermal impedance. |
| $Z^{\text{tsl}}_{\text{ocean}}$ | Thermal impedance of the ocean's wave-mixed turbulent surface layer (tls) of a few meters thick. |
| $Z^{\text{mix}}_{\text{ocean}}$ | Thermal impedance of the ocean's sunlight absorbing, well-mixed near-surface layer of about 100m thick. |
| $Z^{\text{deep}}_{\text{ocean}}$ | Deep ocean thermal impedance where no light penetrates. |
| $Z_{\text{ocean}}$ | Total thermal impedance of the ocean. |
| $R^{\text{air}}_{\text{land}}$, $R^{\text{air}}_{\text{ocean}}$ | Air-land surface and air-ocean interface thermal resistances. |
| $R^{\text{trops}}_{\text{ocean-land}}$ | The heat transfer between troposphere air over land and ocean. (Wind at all troposphere altitudes is the heat transfer medium.) |
| $R^{\text{ocean}}_{\text{Earth}}$ | The heat transfer between the ocean's bottom to deep Earth. |
| $R^{\text{space}}_{\text{land}}$, $R^{\text{space}}_{\text{ocean}}$ | Top-of-Atmosphere resistors between stratopause and space. (Because of the very low pressure at these heights, radiation is the dominating heat transfer mechanism. Therefore, they may be removed or represent linearized radiative heat transfer.) |
| $\Delta I^{\text{stratp}}_{\text{land}}$, $\Delta I^{\text{stratp}}_{\text{ocean}}$ | Stratopause net heat flux. |
| $\Delta T^{\text{stratp}}_{\text{land}}$,$\Delta T^{\text{stratp}}_{\text{ocean}}$ | Stratopause temperature change. |
| $\Delta I^{\text{tropp}}_{\text{land}}$, $\Delta I^{\text{tropp}}_{\text{ocean}}$ | Tropopause net heat flux. |
| $\Delta T^{\text{tropp}}_{\text{land}}$,$\Delta T^{\text{tropp}}_{\text{ocean}}$ | Tropopause temperature change. |
| $\Delta I^{\text{trops}}_{\text{land}}$, $\Delta I^{\text{trops}}_{\text{ocean}}$ | Troposphere net heat flux. |
| $\Delta XSAT_{\text{land}}$,$\Delta XSAT_{\text{ocean}}$ | SAT in region X over land and ocean, respectively. |
| $\Delta I_{\text{land}}$, $\Delta T_{\text{land}}$ | Land surface net heat flux and temperature change. |
| $\Delta I_{\text{ocean}}$ | Ocean net heat flux. |
| $\Delta XSST$ | SST in region X. |
| $\Delta I^{\text{tls}}_{\text{ocean}}$ | Ocean turbulent surface layer net heat flux. |
| $\Delta I^{\text{mix}}_{\text{ocean}}$, $\Delta T^{\text{mix}}_{\text{ocean}}$ | Ocean well-mixed layer net heat flux and temperature change. |
| $\Delta I^{\text{deep}}_{\text{ocean}}$, $\Delta T^{\text{deep}}_{\text{ocean}} \approx 0$ | Deep ocean net heat flux and temperature variation. |
| $\Delta I_{\text{Earth}}$, $\Delta T_{\text{Earth}} = 0$ | Deep Earth net heat flux and temperature change. |
| $\Delta T_{\text{space}} = 0$ | Temperature of space is constant. |
| $I_{\text{AHR}}$, $\Delta T_{\text{hab}}$ | Inhabited region AHR and its temperature change. |

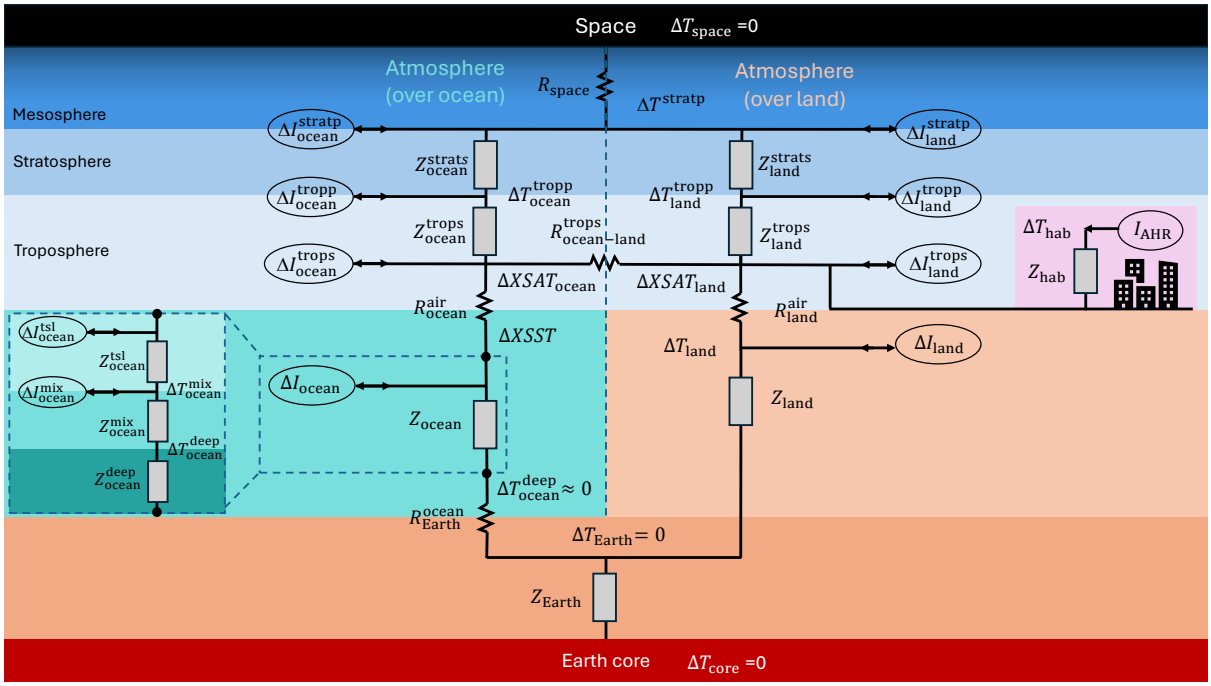


Figure 10: Basic LTI-model for thermal modeling of the Earth thermal system over land and ocean with interaction between both, including an inhabited area with AHR.

# 4 First-order LTI-model for troposphere warming

## 4.1 Model basics

To evaluate the variation in warming over land and ocean globally and in both hemispheres, the multi-Z-box model of Figure 10 is simplified using the methods of section 3.3, into the small-signal model illustrated in Figure 11 with the pre-industrial state of negligible anthropogenic warming $\Delta XSAT_r(1750) = 0$ as a reference state. Because of their large thermal capacitances, the temperatures of the well-mixed ocean layer (but not SST), deep ocean, and deep Earth remain constant on the timescale-of-interest which is 1-to-100 years with a resolution of one year. Diurnal and seasonal temperature variations are not in the scope of interest. The troposphere in the respective VoIs is modeled using the basic scheme of Figure 2 with $T_0 = 0$, VoI-dependent heat sources $I = i_i(t)$ [W/m$^2$], a single capacitor with a VoI-independent thermal capacitance $c_t = 7.3$MJ/Km$^2$ (9) and a single, VoI-dependent resistor $R = r_r$ [Km$^2$/W] characteristic for the heat exchange of that VoI$_r$. This resistor is an effective thermal resistor that represents the complete set of heat transport mechanisms to deep Earth, to deep ocean, to the tropopause, as well as linearized radiative heat exchange with upper layers of the atmosphere and space. For the study at hemispheric scale using the first-order model, the heat exchange between ocean and land will be neglected ($R^{tropp}_{ocean-land} = \infty$) motivated by the large surface area to coast-length ratio for a continent. For smaller regions like Europe and the Arctic, this assumption is invalid. Only the impact of AHR on the average temperature of VoIs will be considered, not the additional local heat island warming.

SST is not constant. Due to the small thermal resistance between water and air related to convective heat transfer ($\sim 0.1$Km$^2$/W), the temperature $\Delta XSST$ of the ocean's wave-mixed surface layer (a few meters thick) follows $\Delta XSAT_{ocean}$. The 100m thick deeply lying, well-mixed ocean layer has a thermal capacity $c^{mix}_{ocean}$ about 40-times the troposphere's capacity. Its temperature $\Delta T^{mix}_{ocean}$ may start to rise slightly on the timescale-of-interest. The first-order effect of increasing $\Delta T^{mix}_{ocean}$ is a reduction of heat transfer between the troposphere and the well-mixed ocean layer due to a smaller temperature difference between them. An increase in

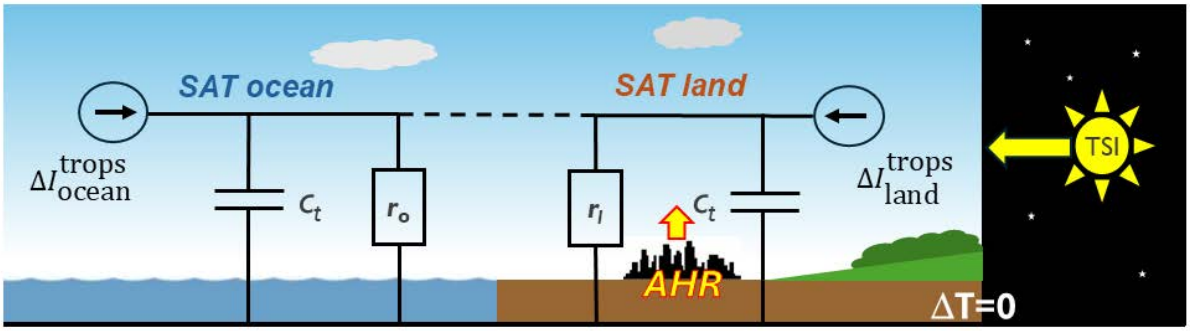


Figure 11: First-order small-signal lumped thermal impedances for the average thermal response calculation over land (SAT land), and over ocean (SAT ocean).

ocean temperature $\Delta T_{\text{ocean}}$ will add to the GSAT per $\Delta GSAT_{\text{ocean}} = \Delta T^{\text{trops}}_{\text{ocean}} + \Delta GSST_{\text{ocean}}$. Hence, assuming a constant temperature of the well-mixed ocean layer ($\Delta T^{\text{mix}}_{\text{ocean}} = 0$) yields a slight underestimation of the GSAT-anomaly $\Delta GSAT$ on the timescale of a century or more.

On land, the sun's radiation is absorbed in a thin surface layer with a small thermal capacitance that can be neglected. The cooling by heat conduction to the very large thermal capacity of deep Earth is incorporated in the thermal resistor $r_{\text{land}}$.

We focus on the pseudo-stationary solution ($c \approx 0$), i.e., the stationary temperature that would be obtained within a period $\Delta t = 3$ to $5\tau$ if the heat source is kept constant at the value reached at time $t$. The net small-signal heat source $\Delta XI^{\text{trops}}_r(t)$ for a specific VoI of the troposphere can be written as

$$\Delta XI^{\text{trops}}_r(t) = XIRTA_r(t) + XAHR_r(t) + XSITA_r(t) \tag{17}$$

with $X = N$ or $S$ indicating the Northern or Southern hemisphere, respectively, and $r$ indicating land or ocean. The following anthropogenic heat sources [W/m$^2$] are included:

- $XIRTA_r(t) = IRTA(t)$: The small signal, IR-heat source in the troposphere resulting from the emission of anthropogenic GHG which is dominated by the emission of $CO_2$. IRTA includes the increase in thermal resistance $r_r$ from its reference value due to the greenhouse effect. Therefore, in first-order, IRTA is assumed to be region independent and to increase at the same rate as the $CO_2$-concentration, i.e., an exponential growth rate with base $a_{\text{IRTA}} = a_{\text{GHG}} = 1.0188$. The IRTA-contribution to global warming is derived by fitting the Southern ocean's SAT-anomaly with

$$\begin{aligned} \Delta SSAT_{\text{ocean}}(t) &= \Delta SSAT_{\text{IRTA}}(2025) \cdot a_{\text{GHG}}^{(t-2025)/1\text{y}} \\ &= (0.77 \pm 0.05) \cdot 1.0188^{(t-2025)/1\text{y}} \text{ K} \end{aligned} \tag{18}$$

  This is justified because the SAT-anomaly over the Southern Hemisphere's ocean is nearly entirely due to IRTA with zero AHR-contribution over the ocean and only a small SITA-contribution because of the low level of ACE in the Southern Hemisphere and ACE's rapid decay. This assumption is corroborated by the exponential base $a_{\text{SSAT}_r} = 1.0207$ of $\Delta SSAT_{\text{ocean}}(t)$ being only slightly larger than $a_{\text{GHG}} = 1.0188$. Any residual AHR or SITA contribution in this region would reduce the inferred IRTA magnitude, making our SITA-estimates conservative. From Equation [18] the $IRTA(t)$ can be derived as

$$IRTA(t) = \frac{\Delta SSAT_{\text{IRTA}}(2025) \cdot a_{\text{GHG}}^{(t-2025)/1\text{y}}}{r_{\text{S-ocean}}} = \frac{0.77 \pm 0.05}{r_{\text{S-ocean}}} \cdot 1.0188^{(t-2025)/1\text{y}} \text{ W/m}^2 \tag{19}$$

  with $r_{\text{S-ocean}}$ the thermal resistance of the troposphere over the ocean in the Southern Hemisphere.

- $XAHR_r(t)$: Region-dependent AHR. $XAHR_r(t)$ is obtained from Equation (14) and Figure 7 with $XAHR_{\text{ocean}} = 0$.

- $XSITA_r(t)$: Region-dependent, small-signal heat source for the troposphere related to a change in its solar irradiation absorption. Motivated by the observed exponential growth of regional SAT-anomalies exceeding that expected from IRTA/GHG and AHR alone, and the evidence of rapidly increasing ACE exceeding significantly GHG and AHR growth rates, see section 2.4, we represent SITA as an exponentially increasing contribution

$$XSITA_r(t) = XSITA_r(t_0) \cdot a_{\text{XSITA}}^{(t-t_0)/t_r} \tag{20}$$

with a region-specific growth rate defined by base $a_{\text{XSITA}}$. The inference of SITA is driven by the mismatch in growth rates rather than by residual magnitude alone. The emission of anthropogenic chemicals over the ocean is negligible, but airborne chemicals will diffuse from land to ocean, causing an increase in $\Delta XSAT_{\text{ocean}}^{\text{SITA}}$ before decomposing. Hence, the $XSITA_{\text{ocean}}$ heat source over the ocean is modeled as a fraction of the SITA over nearby land with the same exponential base $a_{\text{XSITA}}$

$$XSITA_{\text{ocean}}(t) = F_{\text{Xlo}} \cdot XSITA_{\text{land}}(t_0) \cdot a_{\text{XSITA}}^{(t-t_0)/t_r} = XSITA_{\text{ocean}}(t_0) \cdot a_{\text{XSITA}}^{(t-t_0)/t_r} \tag{21}$$

with $0 \leq F_{\text{Xlo}} \leq 1$. $XSITA_r(t)$ will be obtained by fitting to $\Delta XSAT_r$-data.

This set of anthropogenic heat sources for a specific VoI is complete, i.e., there are no other small-signal heat sources contributing to the troposphere's warming, assuming that variations in cosmic radiation absorption in the troposphere can be neglected. The VoI exchanges heat with its surroundings proportional to $\Delta XSAT_r$ through the effective thermal resistance $r_r$ which includes conductive, convective, radiative, latent (condensation) and mass transfer (rainfall) components. The anthropogenic warming $\Delta XSAT_r(t)$ in region $X_r$ can then be written as

$$\Delta XSAT_r(t) = r_r \cdot [XIRTA_r(t) + XAHR_r(t) + XSITA_r(t)] \tag{22}$$

## 4.2 Estimating the thermal resistance of the troposphere

To determine the thermal resistance $r_r$ in Equation (22), the thermal response of the troposphere to the 11-year solar cycle induced TSI-variation is used to estimate the global effective thermal resistance $r_{\text{G}}$ of the troposphere

$$r_{\text{G}} = 0.29 r_{\text{land}} + 0.71 r_{\text{ocean}} \tag{23}$$

i.e., the area weighted average of the effective thermal resistance over land $r_{\text{land}}$ and over ocean $r_{\text{ocean}}$. In this first-order modeling, we will assume that the thermal resistance over land $r_{\text{land}}$ and ocean $r_{\text{ocean}}$ is region independent over the globe.

The 11-year period fits well within the timescale-of-interest. The work of Camp and Tung [9] provides data on the GSAT-variation induced by the TSI-variation $\Delta TSI$ for the period 1959-2004 which amounts to $\Delta GSAT(\Delta TSI) = 0.2$K. The troposphere absorbed solar irradiance variation due to the 11-year solar cycle can be expressed as

$$\Delta i_{\text{t}} \sin(\omega t) = \frac{\Delta TSI}{TSI} i_{\text{t}} \sin(\omega t) \tag{24}$$

with $i_{\text{t}} = 64\text{W/m}^2$ the TSI-fraction absorbed in the troposphere and $\omega = 18\text{nHz} = 0.57\text{y}^{-1}$, corresponding to a period of 11 years. Using the concept of complex impedance applied to the circuit shown in Fig. 2, the thermal response of the troposphere to the solar cycle can be written as

$$\Delta GSAT \cdot \sin(\omega t + \phi) = z \Delta i_{\text{t}} \sin(\omega t) = |z| \Delta i_{\text{t}} \sin(\omega t + \phi) \tag{25}$$

with

$$z = \frac{\frac{r}{j\omega c}}{r + \frac{1}{j\omega c}}, |z| = \frac{r}{\sqrt{1 + (\omega cr)^2}}, r = \frac{|z|}{\sqrt{1 - (\omega c|z|)^2}}, \text{ and } \phi = \arctan(-\omega cr) \tag{26}$$

$z$ represents an effective, small-signal impedance of the troposphere and must not be interpreted as an equilibrium climate sensitivity. The amplitude of the troposphere's thermal impedance $|z|$ can be obtained from

$$|z| = \frac{\Delta GSAT}{\Delta i_t} = \frac{\Delta GSAT}{\Delta TSI}\frac{TSI}{i_t} = \kappa\frac{TSI}{i_t} \tag{27}$$

Camp and Tung's [9] analysis yields $\kappa = \Delta GSAT/\Delta TSI = 0.18 \pm 0.08 \text{Km}^2/\text{W}$ or $\Delta GSAT = \kappa\Delta TSI = 0.11 \pm 0.05\text{K}$. In a later analysis, Tung and Camp [39] obtained a more accurate value of $\kappa = 0.17 \pm 0.04 \text{Km}^2/\text{W}$. Further analyses [39–41] yield values for $\kappa$ in the range $\kappa = 0.07$ to $0.14 \text{Km}^2/\text{W}$.

The impact analysis of the 11-year periodic TSI-variation on GSAT is hindered by the presence of GSAT-variations unrelated to the TSI-variation under study, such as the El Niño-Southern Oscillation and the global warming trend itself. Additionally, TSI-variations with longer and shorter periods interfere with the 11-year periodic variation. Different methods have been applied to filter out these disturbing temperature data mainly by using data from specific years only [9, 39–41]. This elimination of data as well as the resulting incomplete filtering of GSAT-variations not related to the 11-year solar cycle, are expected to result in an underestimation of $\kappa$.

As an alternative approach, we transformed the GSAT and TSI signals [9] into the frequency domain using all data-points and sent them through a band-pass filter located at $\omega = 0.57$ year$^{-1}$ with width $\Delta\omega = 0.33$ year$^{-1}$ equal to the width of the 11-year TSI-peak in the frequency domain, see Figure 3. The resulting signals are back-transformed to the time-domain. The filtered TSI-signal was then scaled to fit the filtered GSAT-signal. According to equation (27), the scaling factor is equal to $\kappa$. A least-squares (LS) fit yields $\kappa = 0.19 \pm 0.04 \text{Km}^2/\text{W}$, and hence $\Delta GSAT = \kappa\Delta TSI = 0.11 \pm 0.02\text{K}$ with the uncertainty specified by two standard deviations. This result corresponds well with the high sensitivity results of Camp and Tung [9, 39]. The large deviation of the scaled, filtered TSI-signal with respect to the thermal response around the year 2000 gets a lot of weight in a least-squares fit. Since this deviation is not related to the 11-year period TSI-variation and tends to underestimate $\kappa$, we also used a robust Median Absolute Deviation (MAD) and rank correlation based fitting method. This yields $\kappa = 0.23 \pm 0.07 \text{Km}^2/\text{W}$, and $\Delta GSAT = \kappa\Delta TSI = 0.13 \pm 0.04\text{K}$.

In the remainder of this paper, we will use the midpoint value $\kappa = 0.21 \pm 0.02 \text{Km}^2/\text{W}$. Its uncertainty is determined by the LS and MAD fit values. Appendix A provides the model results for all three values of $\kappa$. Figure 12 shows the original and the filtered $\Delta TSI$ and $\Delta GSAT$ data, together with the LS-based fit curve ($\kappa = 0.19 \text{Km}^2/\text{W}$), the MAD-based fit curve ($\kappa = 0.23 \text{Km}^2/\text{W}$), and the intermediate response curve $\Delta GSAT = 0.21\Delta TSI$. Because of its small size, the phase shift is not used in the modeling and is set equal to zero for the intermediate fit $\kappa = 0.21$.

The filtering method isolates the strongest TSI-variation signal component together with its thermal response. These signal components are physically coupled by the thermal impedance of the troposphere $z$. This filtering method more effectively eliminates SAT-components that are not related to the 11-year solar cycle. Therefore, it is expected to yield an improved estimation of $\kappa$ than those obtained by previously used methods [9, 39–41].

With $\kappa = 0.21 \pm 0.02 \text{Km}^2/\text{W}, \omega = 18\text{nHz}$, $c_t = 7.3 \text{MJ}/\text{Km}^2$, Equations (26) and (27) yield the global average troposphere thermal impedance

$$|z_G| = 4.4 \pm 0.5 \text{ Km}^2/\text{W}, \; r_G = 5.4 \pm 0.9 \text{ Km}^2/\text{W}, \text{ and } \tau_G = r_G c_t = 1.3 \pm 0.2 \text{ year} \tag{28}$$

with $\tau_G$ the global relaxation time-constant for the troposphere's thermal response. The phase

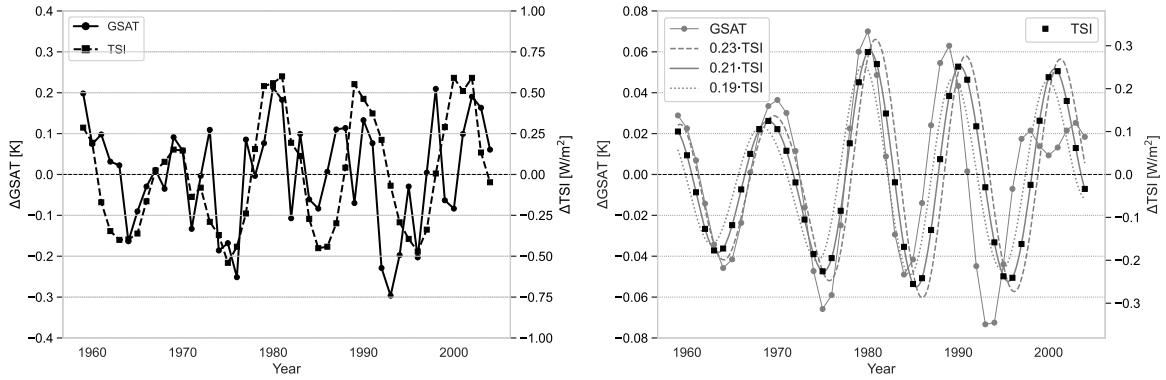


(a) GSAT and TSI between 1959 and 2004 [9].

(b) Band-filtered GSAT and TSI signals.

Figure 12: Signal processing of TSI and GSAT signals [9] to obtain $\kappa$. Scaled TSI-fits to the filtered $\Delta GSAT$-values for $\kappa = 0.19$, $\kappa = 0.21$, and $\kappa = 0.23\text{Km}^2/\text{W}$ are shown in Fig. 12b.

shift between solar cycle irradiance and the temperature response is approximately

$$\phi = \arctan(-\omega c_t r_G) = \arctan(-\frac{2\pi(1.3\text{y})}{11\text{y}}) = -36^\circ \tag{29}$$

or a delay of about a year. This is consistent with the indiscernible phase shift between the TSI-variation and the GSAT-variation caused by it.

The precision of the determination of $\kappa$ can be further improved by using larger TSI/SAT-datasets and associated optimization of the band filter's width and position. By evaluating the spatial variance of $\Delta GSAT(\Delta TSI, r)$ it can be extended to establish the latitudinal variations of $\kappa(r)$ and its value over land $r_{\text{land}}$ and ocean $r_{\text{ocean}}$ separately. Additionally, the annual variation of solar irradiance at different latitudes could be used to establish the position-dependent $\kappa(r)$ more accurately. This is beyond the scope of this paper.

$r_{\text{ocean}}$ cannot be simply obtained by fitting Equation (22) to SAT-data. From the observed SAT, we assume that the contribution of SITA to anthropogenic warming is negligible up to about 1990. Under this assumption and for a given value of $r_G$, the value of $r_{\text{ocean}}$ must fall in a narrow range to give consistent results for the magnitude of the regional SITA-sources and their global and hemispherical averages, i.e, $XSITA_{\text{ocean}} < XSITA < XSITA_{\text{land}}$. For a given $r_G = 5.4\text{Km}^2/\text{W}$, consistency is obtained with $r_{\text{ocean}} = 5.25 \pm 0.05\text{Km}^2/\text{W}$. Finally, the effective thermal resistance $r_{\text{land}}$ of the troposphere over land can be obtained from Equation (23)

$$r_{\text{land}} = \frac{r_G - 0.71 r_{\text{ocean}}}{0.29} = 5.9 \pm 0.9\text{Km}^2/\text{W} \tag{30}$$

with $2\sigma \approx 17\%$ the uncertainty.

The thermal resistance for the heat transfer air and deep ocean is expected to be smaller than that for the heat transfer between air and deep Earth for several reasons:

- The convective heat transfer between air and ocean is higher than between air and land because the average wind speed over the ocean is higher than over land and waves increase the effective interface area for convective heat transfer.
- Water evaporation, which is limited over land, is a heat transfer contributor which further lowers the resistance to heat exchange between the troposphere and ocean. [3].
- The thermal resistance of convective heat transport between the ocean surface and deep ocean is expected to be lower than the thermal resistance of conductive heat transport between land surface and deep Earth.

This implies $r_{\text{ocean}} < r_{\text{G}} < r_{\text{land}}$ and a higher temperature impact over land than over ocean for the same heat flux, see Equation (22). In addition to a difference in heat fluxes, the difference in warming over land and ocean is a matter of different thermal resistances, not a difference in thermal capacitance.

### 4.3 First-order LTI-model results

Equation (22) can be written as

$$\begin{aligned} \Delta XSAT_r(t) = r_r IRTA(2025) a_{\text{GHG}}^{(t-2025)/1\text{y}} \\ + r_r XAHR_r(2025) a_{\text{XAHR}_r}^{(t-2025)/1\text{y}} + r_r XSITA_r(2025) a_{\text{XSITA}_r}^{(t-2025)/1\text{y}} \end{aligned} \tag{31}$$

$$\begin{aligned} \Delta XSAT_r(t) = \Delta XSAT^{\text{IRTA}}(2025) \cdot 1.0188^{(t-2025)/1\text{y}} \\ + \Delta XSAT_r^{\text{AHR}}(2025) a_{\text{XAHR}_r}^{(t-2025)/1\text{y}} + \Delta XSAT_r^{\text{SITA}}(2025) a_{\text{XSITA}_r}^{(t-2025)/1\text{y}} \end{aligned} \tag{32}$$

With $r_{\text{S-ocean}} = r_{\text{ocean}} = 5.25\ \text{Km}^2/\text{W}$, the globally uniform contribution of IRTA to global warming can be derived from Equation (19)

$$\begin{aligned} IRTA(t) = IRTA(2025) \cdot a_{\text{GHG}}^{(t-2025)} = \frac{\Delta SSAT_{\text{ocean}}(t)}{r_{\text{ocean}}} \\ = (150 \pm 30) \cdot 1.0188^{(t-2025)}\ [\text{mW/m}^2] \end{aligned} \tag{33}$$

The region-dependent heat sources $XAHR(t)$ of Equation (31) are obtained from the primary energy consumption data [19] given in Figure 7.

With known thermal resistances $r_r$, the magnitude and growth rate of $\Delta XSAT_r^{\text{SITA}}(t)$ are obtained by fitting the model (31) simultaneously to the regional exponential SAT-trends (1) of Figure 1, after accounting for the contributions of IRTA and AHR. This approach yields more accurate results than fitting directly to the experimental SAT-data since it reduces the influence of the 66-year SAT-oscillation and the SAT-data spread around the warming trend. This fitting procedure isolates the residual warming component required to reproduce the observed SAT-dynamics under the first-order LTI-model's assumptions. The resulting SITA-contribution should be interpreted as an effective heating term. It is not derived from direct measurements of solar absorption by ACE. This approach yields the following regional SITA-contributions $[\text{mW/m}^2]$:

$$\begin{aligned} NSITA_{\text{land}}(t) &= NSITA_{\text{land}}(2025) \cdot a_{\text{NSITA}}^{(t-2025)} = (120 \pm 10) \cdot (1.11 \pm 0.01)^{(t-2025)} \\ NSITA_{\text{ocean}}(t) &= NSITA_{\text{ocean}}(2025) \cdot a_{\text{NSITA}}^{(t-2025)} = (90 \pm 10) \cdot (1.11 \pm 0.01)^{(t-2025)} \\ SSITA_{\text{land}}(t) &= SSITA_{\text{land}}(2025) \cdot a_{\text{SSITA}}^{(t-2025)} = (74 \pm 8) \cdot (1.033 \pm 0.005)^{(t-2025)} \\ SSITA_{\text{ocean}}(t) &= SSITA_{\text{ocean}}(2025) \cdot a_{\text{SSITA}}^{(t-2025)} = (10 \pm 4) \cdot (1.033 \pm 0.005)^{(t-2025)} \end{aligned} \tag{34}$$

with two standard deviations ($\pm 2\sigma$) indicating the uncertainty of the fit results with the given thermal resistance values (30), $IRTA(t)$, and $XAHR_r(t)$, i.e., without the uncertainties on these values themselves.

Figure 13 shows the model results for the SAT-anomalies in the different regions-of-interest for the period 1850-2025 and the evolution of the warming contributors IRTA, AHR, and SITA. Figure 14 gives the contributions to the SAT-anomaly $\Delta XSAT_r$ of IRTA, AHR, and SITA for 2025.

### 4.4 SITA warming trend

The SITA-warming corresponds to an increase in SITA of close to 0.2% over land in the Northern Hemisphere, see Equation (34) and Section 2.4. In the Southern Hemisphere, SITA-warming

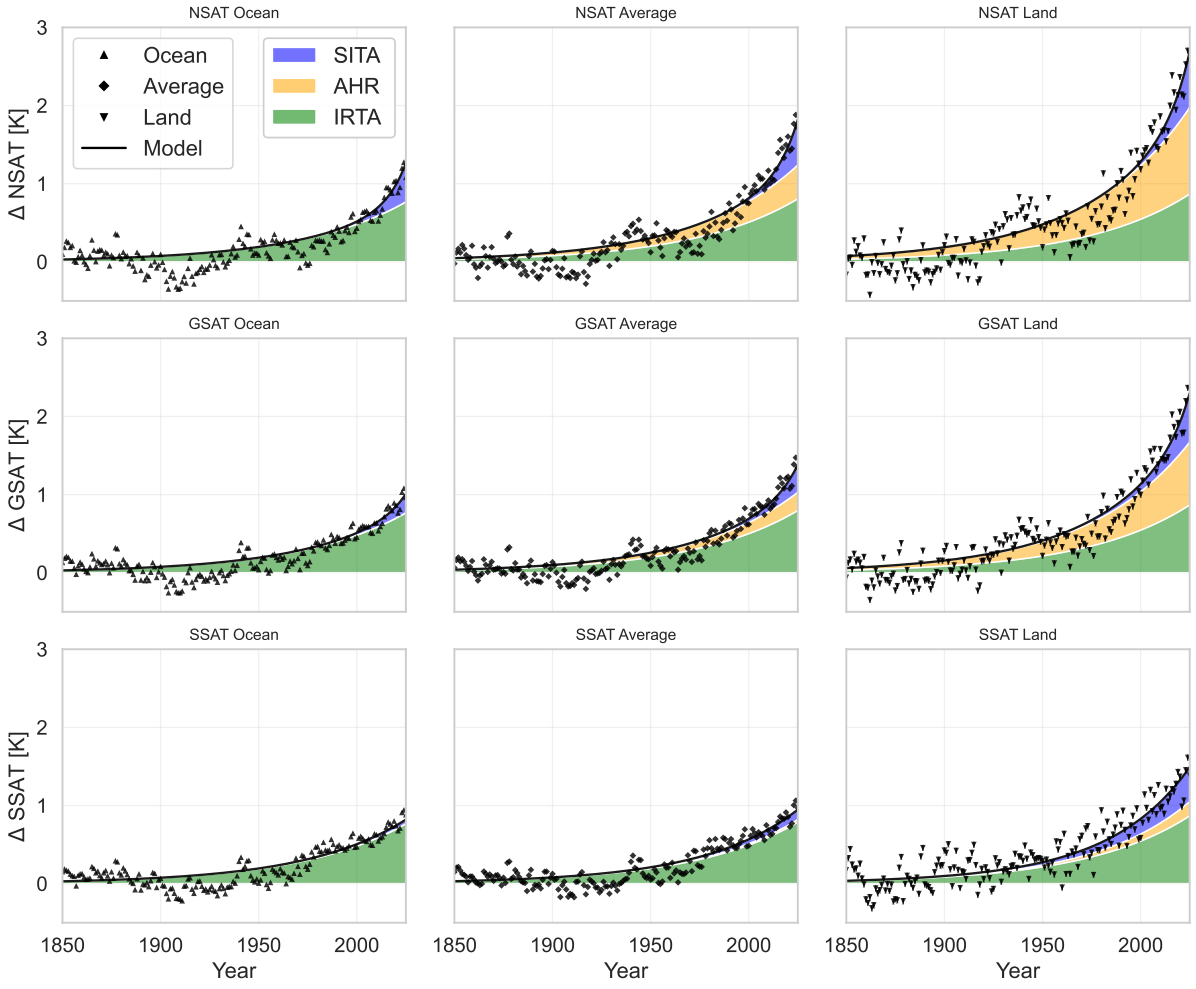


Figure 13: SAT-anomalies globally and for both hemispheres over land, ocean, and for the land-ocean average with modeled troposphere warming contributions including IRTA (green), AHR (yellow), and SITA (blue).

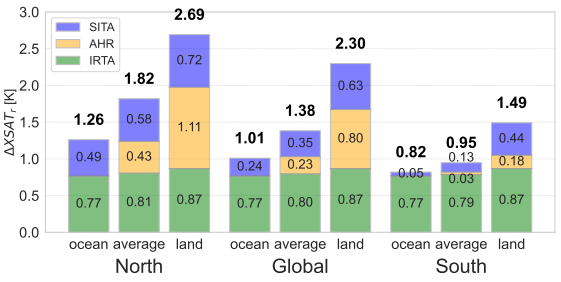


(a) $\Delta XSAT_{\rm r}$ contributions in 2025.

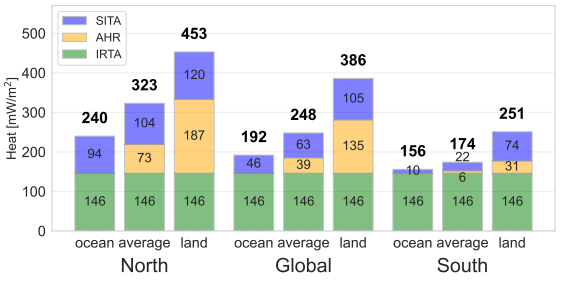


(b) Heat contributions in 2025.

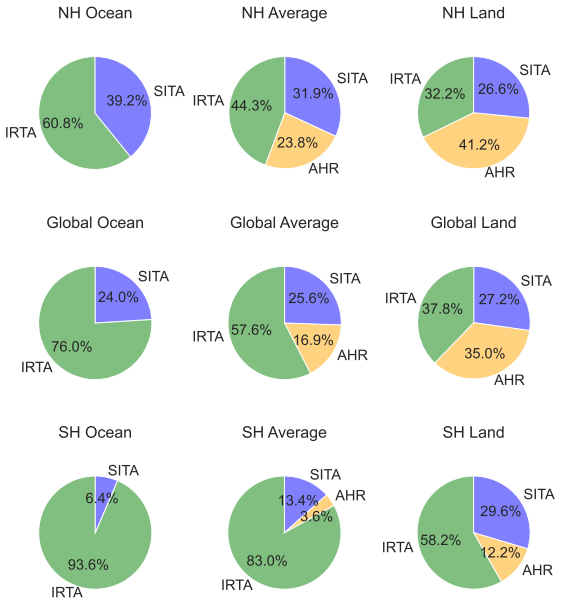


(c) Relative SAT contributions to warming in 2025.

Figure 14: Charts giving the 2025 warming contributions from IRTA/GHG, AHR, and SITA/ACE for different regions based on $\kappa = 0.21$ Km$^2$/W estimate.

is very limited over the ocean but already significant over land, where it increases at a rate of more than 3% per year. In the Northern Hemisphere SITA increases three times as fast and has a significant warming contribution over the Northern Hemisphere's oceans. The SITA-increase rates of 3.3% per year (Southern Hemisphere) and 11% per year (Northern Hemisphere) encompass the growth rates of plastic production (4.9% per year) and China's NMVOC (8.5% per year) supporting the SITA/ACE-hypothesis. The difference in SITA-increase rates may be a consequence of differences in composition of the chemical burden between both hemispheres related to the differences in industrial activity, agriculture, population and consumption patterns. The location and timing of the enhanced SAT-increase rate are consistent with the locations of the largest chemicals emissions.

Figure 15 shows the different $\Delta XSAT_r$-curves minus the modeled IRTA and AHR warming contributions. What remains are naturally-caused variations and the SITA-warming. Note that this warming trend opposes the expected TSI-induced cooling indicated by the 66-year solar cycle curve. Figure 15 shows that the statistically significant global increase in SITA $\Delta GSAT^{\rm SITA}$ since 1990 coincides temporally with the observed increase (+9% between 1980 and 2014) of hydroxyl-radicals (OH) [2] which is an indicator of large-scale changes in atmospheric chemistry. This temporal correspondence is consistent with, but does not prove, a causal link between ACE and the enhanced SITA. The OH-anomaly is strongly correlated with the SITA-component $\Delta GSAT^{\rm SITA}(t)$ but not with the total GSAT-anomaly $\Delta GSAT(t)$. This indicates that the OH-anomaly is not a consequence of global warming but may be a proxy for the cause of the additional SITA-warming being ACE. These observations strengthen the SITA/ACE-hypothesis.

Figure 1 shows that $\Delta NSAT_{\rm ocean}$ increases the fastest of all temperature anomalies, i.e., the exponential base $a_{\rm NSAT_{ocean}} = 1.037$ is the largest of all regions. The SAT-increase over the ocean of the Northern Hemisphere resulting only from the rapid increase in air-borne chemicals and slower increasing IRTA/GHG in the absence of AHR can explain this. Over land, the combination of IRTA/GHG and additional AHR at a comparable low increase rate and the SITA/ACE increasing at a high rate leads to a lower average land warming rate than over the ocean. A higher concentration of airborne chemicals in the Northern Hemisphere compared

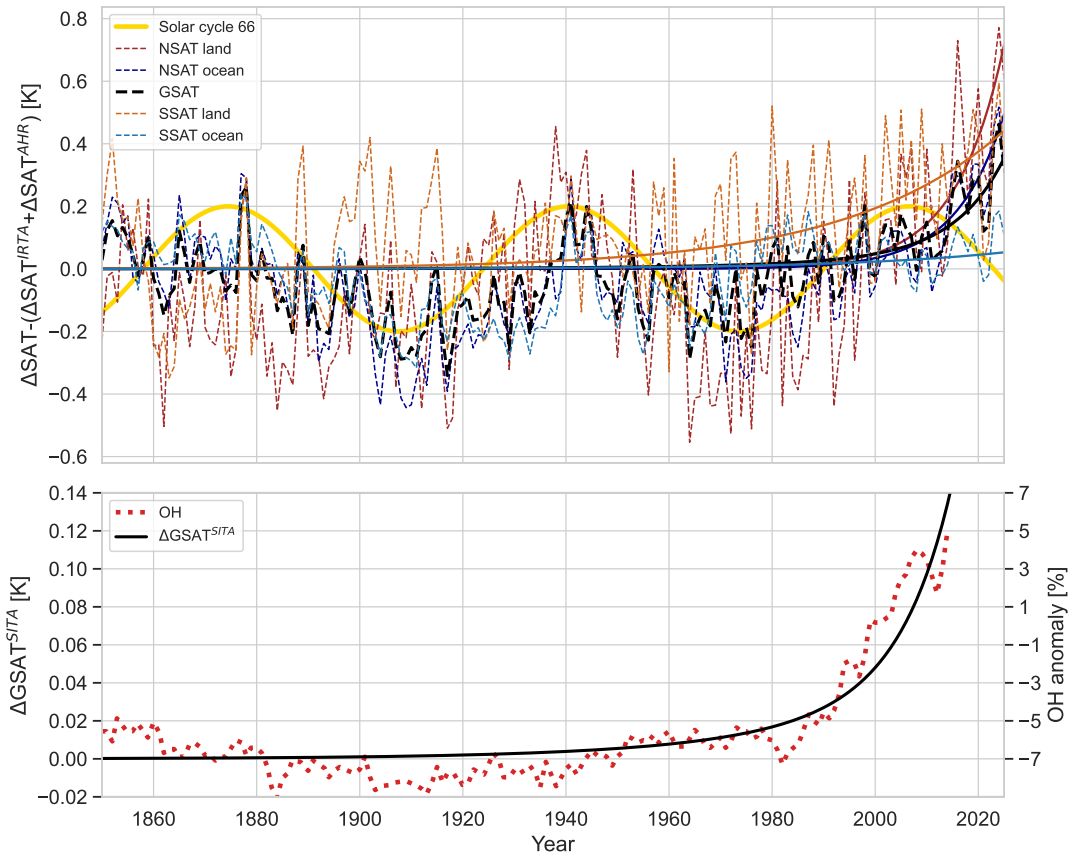


Figure 15: Top: SAT-anomaly of all regions minus the as modeled IRTA/GHG and AHR contributions showing natural SAT-variations and a rapid SITA-heating trend since 1990. The sine curve corresponds to a 66-year period TSI-variation with amplitude of 0.2K (for illustration only). The dashed curves represent the $\Delta NSAT^{\mathrm{SITA}}_{\mathrm{land}}$, $\Delta NSAT^{\mathrm{SITA}}_{\mathrm{ocean}}$, $\Delta NSAT^{\mathrm{SITA}}_{\mathrm{ocean}}$, $\Delta SSAT^{\mathrm{SITA}}_{\mathrm{land}}$, and $\Delta GSAT^{\mathrm{SITA}}$ contributions derived from the SAT-data. The solid curves in the same color show the corresponding $XSITA_r(t)$ models.
Bottom: OH-anomaly increase [2] matching the $\Delta GSAT^{\mathrm{SITA}}$-increase.

to the Southern Hemisphere explains the difference in ocean SAT-increase rates between the hemispheres.

The SITA/ACE-warming hypothesis is based on the physics of light absorption, the sensitivity of troposphere warming to small heat sources in the range of 10-100mW/m$^2$, and on the observed SAT-dynamics implying a troposphere heat source that increases exponentially at a rate significantly higher than 2% per year. It is a working hypothesis that needs further corroboration. The present analysis does not resolve the spectral dependence of absorption, nor does it explicitly model the lifetime and distribution of the chemicals. The SITA-term $\Delta XSAT_r^{\mathrm{SITA}}$ aggregates multiple physical processes, including changes in aerosol burden, chemical composition, and albedo related feedback. Because of its effective forcing nature, it cannot make a distinction between SITA and IRTA effects caused by ACE. However, it is expected that the ACE-contribution is mainly SITA-warming because SITA-warming happens throughout the complete solar irradiation spectrum while the IRTA-effect of ACE is limited to the relatively small atmospheric IR-window.

Similarly, IRTA-quantification using the anthropogenic $CO_2$-emission as a proxy may include some GHG-related SITA-warming.

ACE diffusing into the stratosphere may increase the solar irradiation absorption in the stratosphere by which SITA is reduced and the stratosphere temperature increases. This effect will end-up in a change in IR-radiation from the stratosphere to the troposphere and thus in an IRTA-change. Because most ACE is short-lived, the role of the stratosphere in troposphere warming is expected to be small.

The primary result shown here is that the observed regional SAT-dynamics requires an additional rapidly increasing tropospheric heat source besides IRTA/GHG and AHR for its explanation. Identifying the physical and chemical origins of this source implies detailed analysis of the atmospheric chemical composition and its spectrally resolved impact on the troposphere's transparency and IR-heat exchange. The role of diminishing aerosol concentrations, albedo changes, and TSI-variations, all SITA-effects, must be included in this detailed modeling.

### 4.5 Heat island modeling

AHR is generated in inhabited regions, typically in a VoI consisting of a 100m thick layer of air near the Earth's surface that has a thermal capacitance $c_s \approx 100\mathrm{kJ/Km^2}$. Concentrated emission of AHR implies an additional heat-spreading resistance $r_s$ to be taken into account to obtain the SAT-increase in the inhabited region-of-interest. It is a characteristic of the AHR-source and its environment. It results in an additional SAT-increase $\Delta SAT_{\mathrm{hab}} = r_s AHR_r(t)$ in the region-of-interest on top of the SAT-increase $\Delta XSAT_{\mathrm{land}}$ of its surroundings, see Figure 10. $AHR_r(t)$ is the regional AHR dissipated in the inhabited region-of-interest which can be defined at different scales: country, region, or city. The relaxation time for AHR is given by $\tau_{\mathrm{AHR}} = r_s c_s$.

Heat island Belgium has already heated 3K since 1880 [42]. The average total primary energy consumption in Belgium in the last decade amounts to 2.5EJ/year [19] or 79GW, which corresponds to a $AHR_B = 2.65\mathrm{W/m^2}$ or more than 70-times $GAHR$. Belgium's extra heat is dissipated through a heat spreading resistance $r_{\text{s-B}}$. Belgium's SAT-anomaly $\Delta BESAT$ is about 0.5K higher than Europe's average temperature anomaly $\Delta EUSAT = 2.5\mathrm{K}$ [1], see Figure 16. This yields Belgium's heat spreading resistance

$$r_{\text{s-B}} = \frac{\Delta BESAT - \Delta EUSAT}{AHR_B} = \frac{0.5\mathrm{K}}{2.65\mathrm{W/m^2}} \approx 0.2\mathrm{Km^2/W} \tag{35}$$

The relaxation time for Belgium's AHR-heating is then $r_{\text{s-B}} c_s \approx 20000\mathrm{s} \approx 6\mathrm{hours}$.

# 5 Lumped thermal impedance modeling insights

## 5.1 Accelerating global warming

Foster and Rahmstorf [6] have shown that global warming is accelerating with statistical significance. The leading hypothesis for accelerated global warming is the reduction of aerosol cooling [6] and an increase in ozone level in the troposphere. However, the ozone concentration does not increase at a rate sufficient to explain the observed rapid warming [3]. The aerosol-based explanation suffers from a high degree of quantitative uncertainty. Furthermore, its effect is limited in magnitude and in time as it decreases with decreasing aerosol concentration. The warming effect of reducing aerosol concentrations reaches its upper limit $\Delta XSAT_r^{\text{aero}}(\infty)$ when the aerosol concentration has reached its natural lower limit. Its warming contribution decelerates with time. If the aerosol concentration decreases exponentially by $c_r^a$ % per year, the aerosol warming behaves as

$$\Delta XSAT_r^{\text{aero}}(t) = \Delta XSAT_r^{\text{aero}}(\infty)[1 - (1 + c_r^a)^{-(t-t_0)/t_r}] \tag{36}$$

with an exponentially decreasing instantaneous warming rate given by

$$\delta\Delta XSAT_r^{\text{aero}}(t) = \frac{\partial \Delta XSAT_r^{\text{aero}}(t)}{\partial t} = \Delta XSAT_r^{\text{aero}}(\infty) \ln(1 + c_r^a)(1 + c_r^a)^{-(t-t_0)/t_r} \tag{37}$$

not an exponentially increasing one. From this dynamical analysis, it can be concluded that a reduction in aerosol cooling cannot explain an exponentially increasing warming rate.

The lumped impedance modeling presented here gives a straightforward explanation for the observed warming acceleration. SAT-anomalies $\Delta XSAT_r$ and instantaneous warming rates $\delta\Delta XSAT_r$ increase exponentially because warming is driven by:

- a globally uniform exponential increase in $CO_2$-concentration, reducing exponentially the cooling by IR radiation of the troposphere combined with increasing terrestrial IR absorption (IRTA);
- a region-dependent exponentially increasing AHR in the troposphere;
- a region-dependent exponentially increasing SITA caused by exponentially increasing ACE.

The percentage growth rate of SITA significantly exceeds that of IRTA and AHR. In the last four decades, its warming contribution has become significant. If no measures are taken, it may become the dominant warming agent that further accelerates global warming in excess of a constant percentage per year growth at decadal timescales.

## 5.2 Europe's warming

Europe is warming twice as fast as the global average [4]. Figure 16 shows that in the Northern Hemisphere Europe is not an exception. Actually, Europe's warming since 1990 has been lagging somewhat behind the average SAT-increase over the Northern Hemisphere's land. This may be explained by the fact that Europe's primary energy consumption has not increased substantially in the last 30 years [19], in contrast to the average AHR in the Northern Hemisphere. Before 1990, Europe's SAT-trend coincided with the Northern Hemisphere's SAT-trend. Using a thermal resistance for Europe of $r_{\text{EU}} = 3.1 \pm 0.5 \text{Km}^2/\text{W}$ the first-order IRTA and AHR model contributions can be made to coincide with the Northern Hemisphere ($\text{NSAT}_{\text{land}}$) for that period. Europe's effective thermal resistance $r_{\text{EU}}$ is substantially smaller than the global effective thermal resistance $r_{\text{land}} = 5.9 \text{Km}^2/\text{W}$ for the troposphere over land. Europe's geographical location may provide an explanation for this low resistance. Europe is a large peninsula surrounded by the Mediterranean Sea, the North Atlantic, the Baltic Sea, and the Arctic Ocean, all acting as

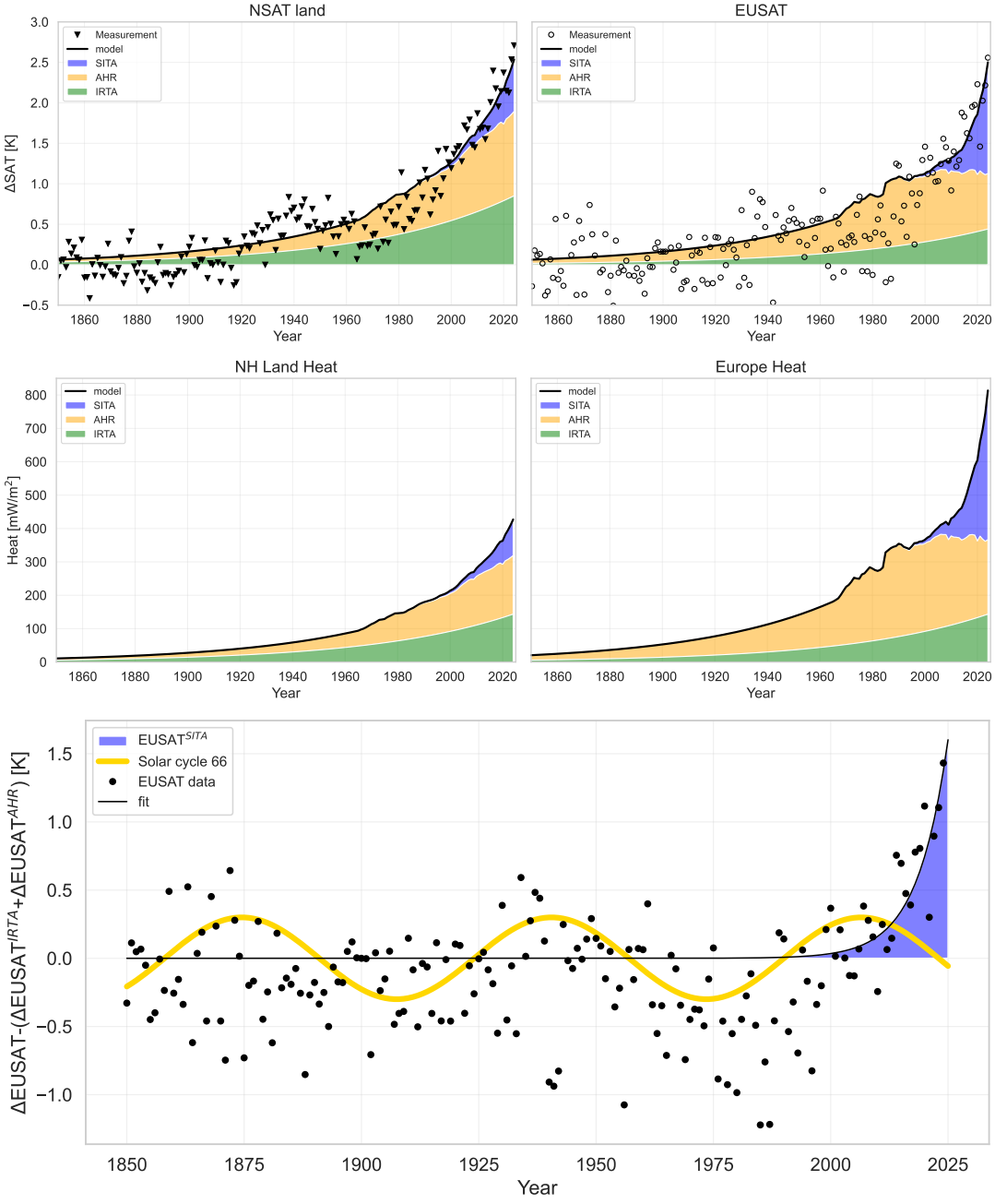


Figure 16: Top: Average SAT-anomaly $\Delta NSAT_{\text{land}}$ over land in the Northern Hemisphere compared to the average SAT-anomaly $\Delta EUSAT$ in Europe (right) [1]. Middle: Average heat fluxes over land in the Northern Hemisphere (left) and in Europe (right). Bottom: Europe's $\Delta EUSAT^{\text{SITA}}$ fitted to $\Delta EUSAT$ minus the IRTA and AHR contributions. Sine curve corresponding to a 66-year period TSI-variation is added for illustration only.

nearby heat sinks for which the heat flow through $R^{\text{trops}}_{\text{ocean-land}}$, see Figure 9, cannot be neglected. Furthermore, the highest concentration of AHR, emitted in the UK, Benelux, and Germany, is located in Europe's coastal regions, see Figure 6. This limits the spreading resistance of Europe's AHR to the surrounding ocean heat sink.

Despite Europe's stagnating energy consumption, Europe is still warming rapidly and seems to catch-up with the average Northern Hemisphere land warming. Europe's SITA-warming is determined by fitting an exponential $\Delta EUSAT^{\text{SITA}}$-model to Europe's SAT-anomaly $\Delta EUSAT(t)$ [1] minus the Europe's IRTA and AHR warming components. This yields

$$\Delta EUSAT^{\text{SITA}}(t) = (1.6\pm0.7)\cdot(1.17\pm0.05)^{(t-2025)/1y}\ [\text{K}] \tag{38}$$

$$EUSITA(t) = \frac{\Delta EUSAT^{\text{SITA}}(t)}{r_{\text{EU}}} = (500\pm200)\cdot(1.17\pm0.05)^{(t-2025)/1y}\ [\text{mW/m}^2] \tag{39}$$

SITA in Europe increases at a rate of approximately 17% per year, which is comparable to but more than the SITA-increase rate in the Northern Hemisphere. In addition to Europe's expected high levels of ACE, two other contributors need to be accounted for:

- The SITA-effect of Europe's reducing aerosol levels temporarily adding to the ACE-warming.
- AHR in Europe is underestimated by the primary energy consumption figures. The waste heat of electricity generation is not entirely included in the primary energy consumption numbers. In the case of renewable electricity generation 100% efficiency is assumed [19]. Solar panels generate 4 to 6kWh of AHR per kWh of electricity, depending on their efficiency (typically 15 to 20% of absorbed sunlight) and the level of albedo reduction they cause. In 2024, Europe generated 1.36EJ of solar power [19] which may represent about 7EJ AHR or about 10% of Europe's primary energy consumption of 71.66EJ. It constitutes 21mW/m$^2$ of extra AHR. The waste heat of solar panels makes up a significant and rapidly growing part of Europe's AHR.

The concentrations of the SLCFs covered by the IPCC-AR6 report [33], specifically NMVOCs, have been decreasing in Europe's air [43]. This indicates that Europe's SITA-warming is caused by other chemical compounds than the NMVOCs covered so far. An in-depth study of the anthropogenic contributors to Europe's rapidly accelerating warming is needed to be able to deploy the proper mitigation measures.

### 5.3 Arctic's warming

Heat flows from high to low temperature. Hence, the Arctic region will function as a heat sink for the AHR of the regions surrounding it: Europe, the Commonwealth of Independent States, and North America. Together, these areas consumed 224EJ of primary energy in 2024. China added another 159EJ [19]. The common temperature inversion above the Arctic implies a higher thermal resistance $r_{\text{ar}}$ in the Arctic region than at lower latitudes. Together with a heat concentration in a smaller area, the Arctic SAT-anomaly $\Delta ARSAT = i_{\text{ar}}/r_{\text{ar}}$ will be higher than in the lower latitude regions surrounding it, consistent with the SAT-observations. Note that the Arctic's SAT-anomaly $\Delta ARSAT = 3\text{K}$ [1] is not much higher than the SAT-anomaly $\Delta NSAT_{\text{land}} = 2.5\text{K}$ over land in the Northern Hemisphere.

AHR that reaches the Arctic will increase the Arctic SAT which, in its turn, will heat up the ice sheet by convective heat transfer $i_{\text{ar}} = h(\Delta ARSAT - T_{\text{sur}})$, with $i_{\text{ar}}$ the heat flux per unit of area to the ice sheet or the Artic's SST at temperature $T_{\text{sur}}$, and $h$ the convective heat transfer coefficient. In this way, AHR directly contributes to the melting of Arctic land and sea ice. To corroborate this view, the amount of energy $E_{\text{m}}$ required to melt the Arctic ice-volume of $V_{\text{m}} = 280 \pm 100\text{km}^3$ that disappears on average each year [44] is calculated.

$$E_{\text{m}} = c_{\text{l}}\cdot\rho_{\text{ice}}\cdot V_{\text{m}} = (333.55\cdot10^3\ \text{J/kg})(917\ \text{kg/m}^3])(280\cdot10^9\ \text{m}^3) = 86\text{EJ} \tag{40}$$

with $c_l$ the latent heat of ice and $\rho_{ice}$ its density. This amounts to 22% of the total AHR dissipated in the Northern Hemisphere [19]. An amount that is only slightly higher than Europe's AHR. This supports the hypothesis that AHR, especially AHR dissipated in Europe because of its northern location, may be an important contributor to the Arctic's extra heating and to the reduction of its ice cover.

In the Antarctic, the same heat sink mechanism applies. However, since the AHR dissipated in the Southern Hemisphere is still limited and since most of the regions with high AHR (Brazil, Australia, Indonesia, South-Africa) are located at much lower latitudes than the AHR releasing regions in the Northern Hemisphere, AHR will not have a significant contribution to the heating of the Antarctic. This is consistent with Antartica's SAT-anomaly of only 0.3K [1].

The effect of a change in albedo, e.g., due to shrinking ice coverage, is significantly different over land than over the ocean. On land, the sun's radiation is absorbed in a thin surface layer of small thermal capacity. This results in a rapid increase in the temperature of the land surface. Therefore, decreasing albedo over land by retracting ice will increase $\Delta SAT_{\text{land}}$ significantly . This creates the well-known positive feedback mechanism that accelerates the melting of the ice sheet. However, in the case of ocean ice, this does not happen. The sun's radiation is not absorbed at the ocean surface but across tens of meters of water that has a large thermal capacity. This implies that on the timescale of tens of years ($c^{\text{mix}}_{\text{ocean}} = 40c_t$, see Figure 3.4), the SST and temperature of the well-mixed ocean layer will hardly change due to a reduced ice coverage ($\Delta T^{\text{mix}}_{\text{ocean}}(t) \approx 0$ at decadal timescale). Since there is less reflected light, the net absorption of sunlight in the atmosphere above an ice-covered ocean reduces with decreasing ice coverage. This results in a temporary, small, negative feedback mechanism that slows down ocean ice-sheet melting on the timescale-of-interest. On the scale of centuries, the well-mixed ocean layer will warm by the increased sunlight absorption resulting in an increasing SST which will overtake this temporary negative feedback mechanism. GCM of the Arctic region that includes AHR inflow from the neighboring landmasses and short-term changes in albedo and ocean temperature is needed to accurately model the Arctic's warming.

### 5.4 The COVID-19 impact

In 2020, the outbreak of COVID-19 led to a global reduction in primary energy consumption of 4% and 8% in Europe [19]. Since a reduced $CO_2$-emission has no immediate effect on the concentration of $CO_2$ in the atmosphere due to its longevity, no reduction in $CO_2$-concentration was measured during the COVID-19 period (2020-2022) [13]. Therefore, as expected, the CovidMIP study by Jones et al. [45] using twelve different Earth system GCMs to predict the impact of COVID-19, none including AHR or SITA/ACE, concluded that no model predicts a significant change in GSAT.

The observations shown in Fig. 17 indicate otherwise. The reduction in global primary energy consumption was followed by a reduction of SAT-anomalies in 2021 of [1]:

- $\Delta GSAT('21) - \Delta GSAT('20) = -0.15$K globally,
- $\Delta NSAT('21) - \Delta NSAT('20) = -0.19$K in the Northern Hemisphere,
- $\Delta NSAT_{\text{land}}('21) - \Delta NSAT_{\text{land}}('20) = -0.23$K over land in the Northern Hemisphere, and
- $\Delta EUSAT('21) - \Delta EUSAT('20) = -0.82$K in Europe.

The one-year delay between AHR and the SAT-dips is consistent with the estimated relaxation time $r_G c_t = 1.3$ year for the troposphere as calculated by the LTI-model, see Equation [28]. Less aerosol pollution in 2020 due to the reduction in industrial activity and transport is expected to result in a SAT-increase due to the reduction of the aerosol cooling effect [3]. This contradicts observations and may indicate a limited role for aerosols in global warming. The drop in AHR represents [19]:

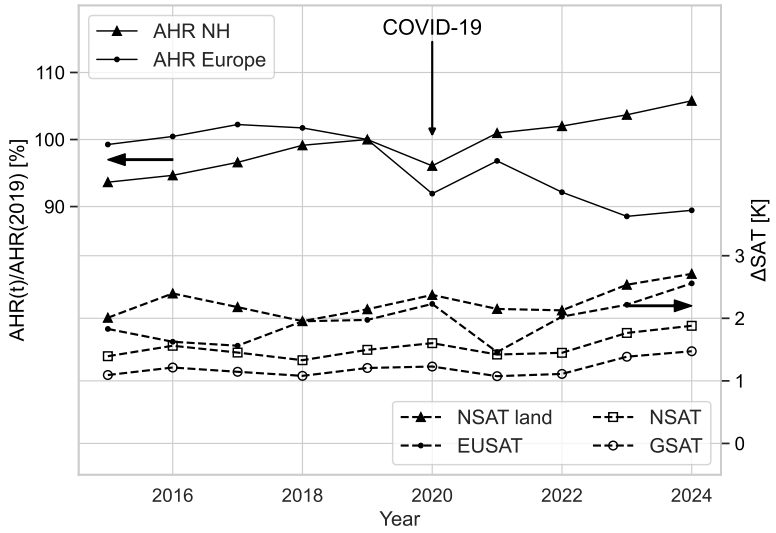


| | ΔAHR [K] | ΔSITA [K] | ΔAHR+ΔSITA [K] | ΔSAT [K] |
|---|---|---|---|---|
| $\delta NSAT_{\text{land-C19}}$ | -0.038 | -0.163 | -0.20 | -0.23 |
| $\delta NSAT_{\text{C19}}$ | -0.015 | -0.135 | -0.15 | -0.19 |
| $\delta GSAT_{\text{C19}}$ | -0.008 | -0.082 | -0.09 | -0.15 |
| $\delta EUSAT_{\text{C19}}$ | -0.062 | -0.372 | -0.43 | -0.82 |

Figure 17: Relative change in AHR [%] in Europe and in the Northern Hemisphere with respect to 2019 [19] versus the SAT-change for Europe $\Delta EUSAT$, Northern Hemisphere land $\Delta NSAT_{\text{land}}$ and globally $\Delta GSAT$ [1] for the period 2015-2024. The arrow indicates COVID-19 outbreak in year 2020. The table shows COVID-19's estimated impact on SAT as a consequence of reduced AHR (ΔAHR) and SITA (ΔSITA) versus SAT-observations (ΔSAT).

- $\Delta GAHR \approx 1.4\text{mW/m}^2$ globally,
- $\Delta NAHR \approx 2.5\text{mW/m}^2$ on average in the Northern Hemisphere,
- $\Delta NAHR_{\text{land}} \approx 6.5\text{mW/m}^2$ over land in the Northern Hemisphere, and
- $\Delta EUAHR \approx 20\text{mW/m}^2$ in Europe.

According to the IPCC-AR6 report [33], Cross-Chapter Box 6.1., COVID-19 led to a 35% reduction of global anthropogenic $NO_x$-emission in April 2020, and 13% to 48% in $NO_2$. Assuming that these reductions are representative of the overall reduction in ACE and its associated SITA, the table at the bottom of Figure 17 gives the expected drop of SAT due to reduced AHR and a reduction of 35% of SITA based on Equations (34) and (38) for 2021. Unlike the GCM-results for the COVID-19 SAT-impact which include only GHG and aerosol forcing [45], the SAT-observations are not inconsistent with the estimated SAT-impact of the AHR and ACE COVID-19 reductions. Natural SAT-variations which are not included in this analysis add to the COVID-19 SAT-impact and may be responsible for the extra cooling of Europe in 2021. It cannot be excluded that the region-dependent global cooling in 2021 is entirely due to COVID-19 unrelated SAT-variations.

# 6 New insights into the dynamics of global warming

## 6.1 The anthropogenic warming mechanism and contributors

Today, global warming has reached a level that allows its temporal and spatial variation to be quantified. Because of the large spatial SAT-anomaly variation, the relationship between continental-scale SAT-anomalies and the spatially varying troposphere heat sources needs to be characterized in addition to the GSAT-anomaly. A dynamic analysis using an LTI-model offers a new way to study the impact of the different heating agents. It can provide insights with first-order quantification of several SAT-dependencies which, thus far, have not been clearly explained quantitatively.

Regionally varying exponentially increasing SAT-anomalies driven by heat sources that significantly increase on a yearly basis (>1% per year), require dynamic thermal modeling that acknowledges the significant heat transfers between the Earth thermal system's components. Top-of-the-atmosphere energy balance methods cannot address this [8]. Global warming at decadal timescales is about dynamic heat flows between the thermal capacitors of the Earth thermal system. It is driven by region-dependent heat sources and sinks varying at different rates that, together with the thermal resistances between the Earth elements and space, determine the temperatures of the Earth thermal system's components. Small dynamic heat sources such as AHR and small changes in solar irradiation absorption in the troposphere, which has a high thermal sensitivity (small thermal capacity, large thermal resistance) cannot be neglected, a priori, in a system that is off-equilibrium.

GCMs can fully capture the dynamics of global warming. However, in most GCM-studies, AHR and SITA heat sources may not have been included. Additionally, GCM's complexity and their level of detail may obscure crucial trends and dependencies. Dynamic analysis on the timescale of a century using the LTI-modeling provides a significantly more nuanced view of anthropogenic global warming than the commonly accepted GHG-centered perspective [3]. Within the framework of the small-signal LTI-model, anthropogenic global warming can be understood as follows.

- Based on the variation of SAT induced by 11-year solar cycle, the troposphere's sensitivity to heat dissipated in it is determined to be $5.4 \pm 0.9$K per W/m$^2$. This is an order of magnitude higher than the SAT-sensitivity attributed by energy balance methods [3]:

$$\frac{\Delta GSAT(2021)}{ERF(2021)} = \frac{1.26\text{K}}{2.84\text{W/m}^2} = 0.44\text{Km}^2/\text{W} \tag{41}$$

- Emission of anthropogenic GHG leads to a uniform increase in GHG globally, resulting in a uniform global warming trend driven by increased net IR absorption in the troposphere. Due to the exponential increase in $CO_2$-concentration, the contribution of GHGs to IRTA/GHG increases exponentially at a rate of 1.88% per year. In 2025, it amounts to $150 \pm 30$W/m$^2$ resulting in $\Delta GSAT^{\text{IRTA}} = 0.8$K or 58% of the total global warming of $\Delta GSAT = 1.38$K in 2025. IRTA/GHG in the troposphere is 20-times smaller than the total anthropogenic top-of-the-atmosphere radiative forcing $ERF = 2.84$W/m$^2$ [3].

- Anthropogenic IRTA/GHG-warming goes together with AHR-warming because both originate predominately from fossil fuel burning. Therefore, both increase at a similar rate of about 2% per year.

- In 2025, AHR contributes $\Delta GSAT^{\text{AHR}} = 0.23$K or 17% to global warming. Over land in the Northern Hemisphere this increases to $\Delta NSAT^{\text{AHR}}_{\text{land}} = 1.1$K, or 41%, exceeding IRTA/GHG-warming of $\Delta NSAT^{\text{IRTA}}_{\text{land}} = 0.87$K. In the Southern Hemisphere AHR's warming contribution is still small but is becoming significant. It contributes $\Delta SSAT^{\text{AHR}}_{\text{land}} = 0.18$K or 12% to the warming over land.

- Until about 1990, the SAT-anomaly evolution and its spatial variation between land and ocean across both hemispheres can be quantitatively modeled using an exponentially increasing, spatially uniform IRTA-component dominated by $CO_2$-concentration increase (IRTA/GHG), and an exponentially increasing, spatially varying AHR-component only.

- Since 1990, a third and until now unacknowledged rapidly increasing anthropogenic heating agent contributes to an exponentially increasing SITA and an accelerating SAT-increase. Exponentially increasing ACE, a type of SLCF, is hypothesized as the source of this increasing SITA. It adds $\Delta GSAT^{\mathrm{SITA}} = 0.35\mathrm{K}$ or 26% to global warming in 2025. This implies that the role of SLCF in global warming other than aerosols has been underestimated thus far. Their warming contribution goes beyond their direct role as GHG or as precursor for direct SLCF [33].

- Unlike the globally uniform IRTA/GHG, AHR and SITA/ACE vary significantly from region to region, in magnitude as well as in their (exponential) increase rate. Spatially varying anthropogenic heat sources lead to spatially varying anthropogenic SAT-anomalies. AHR and SITA are responsible for the differences in SAT-anomalies between the hemispheres, between the Arctic and the Antarctic, and between land and ocean regions. The difference in increase rates in the different regions results in a continuous change of the *relative* contributions of IRTA/GHG, AHR, and SITA/ACE to regional as well as global warming. In 2025, over land in the Northern Hemisphere, the three anthropogenic heating sources IRTA/GHG, AHR, and SITA/ACE are of comparable magnitude. In the Southern Hemisphere IRTA/GHG warming still dominates but AHR and SITA/ACE are at the brink of becoming significant contributors too. Over the ocean, IRTA/GHG warming dominates, with an increasing contribution of SITA/ACE, especially in the Northern Hemisphere.

- AHR and SITA/ACE increase will keep on driving global warming even under zero-carbon-emission conditions. In a GHG emission net-zero situation as of 2050, when GHG-concentrations no longer increase, AHR alone adds 0.6K to $\Delta GSAT(2050)$ by 2100 at today's AHR global average growth rate of 2% per year. In the Northern Hemisphere, AHR will add $\Delta NSAT^{\mathrm{AHR}} = 1\mathrm{K}$ and $\Delta NSAT^{\mathrm{AHR}}_{\mathrm{land}} = 2.7\mathrm{K}$ over land. This is significantly above the predictions of the study of Flanner [18]. If proper measures are not taken, SITA/ACE will add even more heating with a contribution that may increase at a rate in excess of 10% per year, see Figure 15.

The underestimation of the troposphere's temperature sensitivity is responsible for the underestimation of the impact of the AHR and SITA/ACE heat sources in global warming studies.

### 6.2 Model limitations and interpretation

The troposphere LTI-model presented in section 4 is a first-order, physically transparent representation of troposphere warming dynamics on a continental scale. Its primary objective is not to replace general circulation models (GCMs) or comprehensive Earth thermal system models, but to complement them by isolating and quantifying the dynamical response of the troposphere to explicitly defined effective heat sources acting on decadal to centennial timescales. These effective heat sources do not uniquely identify physical mechanisms but aggregate all mechanisms related to IR-radiation absorption (IRTA), solar radiation absorption (SITA), and direct heating (AHR), respectively.

Several limitations of the present approach must be recognized when interpreting the results.

1. The first-order model operates on a continental scale. It represents each continental, troposphere VoI using a single characteristic SAT and eefective thermal impedance assuming an internal quasi-static thermal equilibrium at the timescale-of-interest. Additionally,

on a continental scale, heat exchange between continental land and ocean has been neglected. Therefore, it is not directly applicable to smaller regions, e.g., Europe, or smaller timescales. In such cases, more elaborated LTI-models are required using the same principles as described in section 3.2.

2. The thermal resistances used in the model aggregate multiple physical processes, including convective and conductive heat transfer, latent heat exchange, radiative coupling, and mass exchange. As a result, individual resistance values should be interpreted as effective parameters rather than physical quantities linked to specific heat transport mechanisms. Their numerical values are derived from observed SAT-responses, but they are not uniquely attributable to a single transport mechanism. GCM could calculate effective thermal resistances by aggregating different heat transport mechanisms.

3. The LTI-model partitions the troposphere heating into three components: IRTA, AHR, and SITA. IRTA is parameterized using observed SAT-trends over the Southern Hemisphere's ocean and anthropogenic $CO_2$-concentration growth, under the assumption that this region provides a close approximation to GHG-dominated warming with minimal AHR and SITA influence. While this assumption is physically motivated, it introduces uncertainty that propagates into the estimation of the other components. Independent quantification of the IRTA-warming from physical modeling of the troposphere's change in IRTA would reduce the uncertainty and improve the overall accuracy of the modeling.

4. AHR is derived from the primary energy consumption time series. This provides a lower limit to the actual AHR, because certain contributors to AHR such as the waste heat of renewable energy sources are not included. This impacts the accuracy of the LTI-model.

5. The SITA-contribution identified in this study represents an effective heat source required to reproduce observed SAT-dynamics within the model framework after accounting for IRTA/GHG and AHR. It is derived from the difference between the spatially varying SAT-anomalies and the sum of IRTA/GHG and AHR contributions to these SAT-anomalies. The model does not resolve all the underlying processes. Consequently, the attribution of SITA to ACE should be interpreted as a working hypothesis rather than a definitive causal assignment. The results indicate the presence of an additional rapidly increasing tropospheric heat source consistent with known rapid growth of chemicals production and emissions, but they do not uniquely identify the underlying chemical origin nor quantify the related radiation absorption physics.

6. Interactions among heat sources are treated linearly under a small-signal assumption using a pre-industrial reference state. Feedback processes are implicitly embedded in the observed temperature data used for model calibration and in the LTI-model's parameters but are not explicitly resolved.

7. Internal climate variability and natural oscillatory modes, such as ENSO and longer-period solar variability, are not modeled explicitly. Their influence is mitigated by focusing on long-term trends and the physical relationship between exponentially increasing anthropogenic heat sources and their impact on SAT. Nevertheless, this variability increases the uncertainty on the LTI-model parameters which can be reduced by proper modeling of the natural variations, especially the TSI-variations.

Within these limitations, the strength of the model lies in its ability to demonstrate that the observed magnitude, spatial distribution, and acceleration of SAT-anomalies require consideration of tropospheric heat sources beyond those emphasized in radiative forcing frameworks. The model provides a coherent dynamical interpretation of the observations and first-order quantification of the relationship between SAT-increase and the troposphere warming agents. It generates

testable hypotheses that can be examined using spectrally resolved radiative measurements, chemically explicit atmospheric models, study of the atmosphere's response to TSI-variations as well as to seasonal variations, and targeted GCM-experiments incorporating explicit anthropogenic heat release, atmospheric absorption processes throughout the solar spectrum, and TSI-variations.

The first-order LTI-model of the SAT-anomaly spatial and temporal dependency and the SITA/ACE-hypothesis are testable. The model would require substantial revision if one or more of the following conditions are met:

- Long-term regional SAT-anomalies can be reproduced quantitatively using IRTA/GHG alone, with realistic tropospheric thermal resistances, without requiring additional heat sources.
- Inclusion of AHR in GCM simulations cannot reproduce the spatial and temporal variance of SAT-anomaly until 1990.
- Chemically explicit atmospheric models show that the growth of anthropogenic short-lived compounds cannot produce a net increase in tropospheric solar absorption of order 0.1% or larger.
- Independent attribution analyses demonstrate that the post-1990 acceleration of warming can be fully explained by natural causes, quantified changes in aerosol forcing, internal variability, GHG-forcing or other warming agents.

### 6.3 Warming mitigation recommendations

Climate neutrality requires heat neutrality for the troposphere. It cannot be achieved by carbon neutrality alone. Based on the new insights provided by the first-order LTI-model, the following warming mitigation implications may be considered if the model results are confirmed.

- Energy consumption must be minimized independently of the way energy is generated. Only switching to carbon-free energy generation is insufficient.
- Reduction in the emission of GHGs should not result in an increase in overall energy consumption and extra waste heat generation. In this respect, the low efficiency of carbon-neutral electricity generation (nuclear (35%), solar (<20%), bio (<40%)) must be acknowledged and mitigated. The use or disposal of its waste heat needs to be addressed.
- Wind energy is the only energy vector that does not add net heat to the troposphere. However, it may still create AHR-issues. Importing sea-harvested wind energy to the continent adds to that continent's AHR and SAT.
- The large amount of waste heat generated by solar panels needs to be addressed. The reduction in the albedo of the land's surface by solar panels should be compensated by increasing the albedo at other locations to compensate for the waste heat.
- Waste heat in general, e.g., from power plants and industrial processes, should not be released into the atmosphere. Deep Earth's large thermal capacity could be used as a heat sink.
- Chemical emission reduction measures are urgently required.

The contributions of AHR and SITA/ACE are already significant, but they are not fully taken into account. Since neither AHR nor SITA/ACE create long term effects like $CO_2$-emission does, a significant reduction of the SAT-anomaly can be obtained within a few years when these heating agents are reduced. This is corroborated by the global reduction of SAT after the

COVID-19 crisis, consistent with the reductions of AHR and ACE in 2020. Our analysis suggests that the reduction of AHR and ACE could stop the recent accelerated global warming trend or even lead to a (temporary) reduction of SAT over land in the Northern Hemisphere. This follows directly from the model and should be interpreted as a scenario-dependent implication, not a prediction.

# 7 Conclusion and future work

This paper presents lumped thermal impedance (LTI) modeling as a complementary tool to GCM-modeling. It directly calculates the average temperature of large Volumes-of-Interest (VoI) of the Earth thermal system which results from the heat flow in the LTI-network that represents the VoI and its surroundings with which it exchanges energy. The LTI-method can assess warming of regions of different scales by appropriate LTI-network modeling. A first-order, continental scale LTI-model of the land and ocean parts of the troposphere in both hemispheres is used to quantify the spatial and temporal evolution of SAT-anomalies in response to three effective anthropogenic heat sources: infrared radiation absorption driven by greenhouse gases (IRTA/GHG), direct anthropogenic heat release (AHR), and an additional rapidly increasing effective heat source attributed to changes in solar irradiation absorption within the troposphere (SITA/ACE) related to the rapid increase in anthropogenic chemical emissions (ACE). The model demonstrates that the observed exponential increase in regional SAT-anomalies and their spatial variability between hemispheres, land and ocean, cannot be reproduced by GHG-forcing alone within the LTI-model's framework. When evaluated dynamically, IRTA explains the SAT-anomaly over the Southern Hemisphere's oceans and a substantial fraction of global warming. AHR provides a physically grounded and independently quantifiable contribution that explains the enhanced warming over land and the spatial variance between the hemispheres until about 1990. Later, an additional heat source, more rapidly increasing than IRTA/GHG and AHR, is required to account for the accelerated warming rates observed over land and the Northern Hemisphere's oceans. An effective warming agent SITA/ACE is introduced, whose magnitude and growth rate are derived from the observed SAT-dynamics. The attribution of this heating agent to ACE is proposed as a working hypothesis, supported by the temporal correspondence with the OH-anomaly, a proxy for large-scale changes in atmospheric chemistry, and by the rapid growth of multiple classes of short-lived anthropogenic compounds. The present analysis does not establish causality and does not uniquely identify the underlying chemical species or optical mechanisms.

The principal contribution of this work is the demonstration that tropospheric warming must be analyzed as a dynamic heat-flow problem rather than as an equilibrium surface response to top-of-atmosphere radiative forcing alone. The high thermal sensitivity of the troposphere implies that small, rapidly changing heat sources acting directly within it can have a large, region-dependent contribution to SAT-evolution. This perspective provides a coherent explanation for the spatial and temporal variance of the SAT-anomaly since the industrial revolution and for the region-dependent acceleration of global warming observed over recent decades without invoking additional feedback mechanisms.

Future work should focus on independent empirical validation of the model components. This includes accurate analysis of the total solar irradiation (TSI) time dependency and its impact on SAT to better quantify natural SAT-variations, empirical quantification of the troposphere's thermal sensitivity and its spatial variation by analysis of its thermal response to known TSI-variations, spectrally resolved measurements of atmospheric solar absorption, improved quantification of AHR, and chemically explicit modeling of the radiative impact of short-lived anthropogenic compounds. GCM that explicitly includes AHR, dynamically evolving atmospheric absorption, and realistic timescales of tropospheric heat exchange, is required to further evaluate the hypotheses identified here.

## Acknowledgment

The authors thank Prof. dr. Nicole Van Lipzig of the department of Earth and Environmental Sciences of the KU Leuven, for insightful discussions on the methodologies of climate science and literature references, and dr. ir. Jef Poortmans, imec fellow and part-time professor at the department of Electrical Engineering of the KULeuven, for supporting this work.

## References

[1] NOAA National Centers for Environmental Information (NCEI). Climate at a Glance: Global Time Series, 2026. Dataset retrieved March 21, 2026. URL: https://www.ncei.noaa.gov/access/monitoring/climate-at-a-glance/global/time-series.

[2] S. Szopa, V. Naik, B. Adhikary, P. Artaxo, T. Berntsen, W. D. Collins, S. Fuzzi, L. Gallardo, A. Kiendler-Scharr, Z. Klimont, H. Liao, N. Unger, and P. Zanis. Short-Lived Climate Forcers. In V. Masson-Delmotte, P. Zhai, A. Pirani, S. L. Connors, C. Péan, S. Berger, N. Caud, Y. Chen, L. Goldfarb, M. I. Gomis, M. Huang, K. Leitzell, E. Lonnoy, J. B. R. Matthews, T. K. Maycock, T. Waterfield, O. Yelekçi, R. Yu, and B. Zhou, editors, *Climate Change 2021: The Physical Science Basis. Contribution of Working Group I to the Sixth Assessment Report of the Intergovernmental Panel on Climate Change*, pages 817–922. Cambridge University Press, Cambridge, United Kingdom and New York, NY, USA, 2021. Fig. 6.9, p. 850. URL: https://www.ipcc.ch/report/ar6/wg1/chapter/chapter-6/, doi:10.1017/9781009157896.008.

[3] P. Forster, T. Storelvmo, K. Armour, W. Collins, J.-L. Dufresne, D. Frame, D. J. Lunt, T. Mauritsen, M. D. Palmer, M. Watanabe, M. Wild, and H. Zhang. The Earth's Energy Budget, Climate Feedbacks, and Climate Sensitivity. In V. Masson-Delmotte, P. Zhai, A. Pirani, S. L. Connors, C. Péan, S. Berger, N. Caud, Y. Chen, L. Goldfarb, M. I. Gomis, M. Huang, K. Leitzell, E. Lonnoy, J. B. R. Matthews, T. K. Maycock, T. Waterfield, O. Yelekçi, R. Yu, and B. Zhou, editors, *Climate Change 2021: The Physical Science Basis. Contribution of Working Group I to the Sixth Assessment Report of the Intergovernmental Panel on Climate Change*, pages 923–1054. Cambridge University Press, Cambridge, United Kingdom and New York, NY, USA, 2021. URL: https://www.ipcc.ch/report/ar6/wg1/chapter/chapter-7/, doi:10.1017/9781009157896.009.

[4] C3S-ECMWF and WMO. C3S-WMO European State of the Climate 2025, 2026. URL: https://climate.copernicus.eu/ESOTC/2025, doi:10.24381/zy93-sb27.

[5] Our World in Data. Annual sea surface temperature anomalies relative to the pre-industrial period, 2026. Dataset retrieved March 21, 2026. URL: https://ourworldindata.org/grapher/sea-surface-temperature-anomaly.

[6] G. Foster and S. Rahmstorf. Global warming has accelerated significantly. *Geophysical Research Letters*, 53, 2026. doi:10.1029/2025GL118804.

[7] ISO 2533:1975 Standard Atmosphere, 1975. International Organization for Standardization. URL: https://www.iso.org/standard/7472.html.

[8] G. Lohmann. Temperatures from energy balance models: the effective heat capacity matters. *Earth System Dynamics*, 11:1195–1208, 2020. doi:10.5194/esd-11-1195-2020.

[9] C. D. Camp and K. K. Tung. Surface warming by the solar cycle as revealed by the composite mean difference projection. *Geophysical Research Letters*, 34(14):L14703, 2007. doi:10.1029/2007GL030207.

[10] F. Halberg, G. Cornélissen, K.-H. Bernhardt, M. Sampson, O. Schwartzkopff, and D. Sonntag. Egeson's (George's) transtridecadal weather cycling and sunspots. *History of Geo- and Space Sciences*, 1(2):49–61, 2010. doi:10.5194/hgss-1-49-2010.

[11] G. C. Reid. Solar variability and the earth's climate: introduction and overview. *Space Science Reviews*, 94:1–11, 2000. URL: https://link.springer.com/article/10.1023/A:1026797127105.

[12] Our World in Data. Annual concentration of atmospheric carbon dioxide, 2025. Dataset retrieved March 21, 2026. URL: https://ourworldindata.org/grapher/co2-long-term-concentration.

[13] X. Lan and R. Keeling. Trends in Atmospheric Carbon Dioxide ($CO_2$): Mauna Loa $CO_2$ annual mean data, 2025. Dataset retrieved March 21, 2026; NOAA GML and Scripps. URL: https://gml.noaa.gov/ccgg/trends/data.html.

[14] G. Myhre, E. J. Highwood, K. P. Shine, and F. Stordal. New estimates of radiative forcing due to well mixed greenhouse gases. *Geophysical Research Letters*, 25(14):2715–2718, 1998. doi:10.1029/98GL01908.

[15] NOAA Global Monitoring Laboratory. The noaa annual greenhouse gas index (aggi), 2025. URL: https://gml.noaa.gov/aggi/aggi.html.

[16] Our World in Data. Global warming: annual temperature anomaly (Explorer), 2025. Dataset retrieved March 21, 2026. URL: https://ourworldindata.org/explorers/climate-change.

[17] Our World in Data. Global primary energy consumption by source, 2025. Dataset retrieved March 21, 2026. URL: https://ourworldindata.org/grapher/global-energy-substitution.

[18] M. G. Flanner. Integrating anthropogenic heat flux with global climate models. *Geophysical Research Letters*, 36(2):L02801, January 2009. doi:10.1029/2008GL036465.

[19] Energy Institute. Statistical Review of World Energy 2025, 2025. Dataset retrieved March 21, 2026. URL: https://www.energyinst.org/statistical-review.

[20] A. Kleidon, G. Messori, B. S. Roy, I. Didenkulova, and N. Zeng. Global warming is due to an enhanced greenhouse effect, and anthropogenic heat emissions currently play a negligible role at the global scale. *Earth System Dynamics*, 14(1):241–242, 2023. doi:10.5194/esd-14-241-2023.

[21] I. Khmelinskii and L. V. Woodcock. Editorial Comment on Earth System Dynamics' "Greenhouse Effect" Editorial, 2023. Preprint/commentary; DOI: 10.13140/RG.2.2.12156.00641. URL: https://www.researchgate.net/publication/370156771.

[22] A. Feinberg. Urbanization Heat Flux Modeling Confirms It Is a Likely Cause of Significant Global Warming: Urbanization Mitigation Requirements. *Land*, 12(6):1222, 2023. doi:10.3390/land12061222.

[23] B. Nordell and B. Gervet. Global Warming Is Global Energy Storage. In *Proceedings of the Global Conference on Global Warming (GCGW-08)*, page 561, Istanbul, Turkey, 2008. URL: https://www.diva-portal.org/smash/get/diva2:1011381/FULLTEXT01.pdf.

[24] B. Chen, L. Dong, X. Liu, G. Y. Shi, L. Chen, T. Nakajima, and A. Habib. Exploring the possible effect of anthropogenic heat release due to global energy consumption upon global climate: a climate model study. *International Journal of Climatology*, 36(15):4790–4796, 2016. doi:10.1002/joc.4669.

[25] L. Yan, S. Zheng, and L. Hao. Quantification of anthropogenic heat and simulation of its effect on environment and climate: A comprehensive review. *Renewable and Sustainable Energy Reviews*, 204, October 2024. doi:10.1016/j.rser.2024.114802.

[26] M. Xie, K. Zhu, T. Wang, W. Feng, D. Gao, M. Li, S. Li, B. Zhuang, Y. Han, P. Chen, and J. Liao. Changes in regional meteorology induced by anthropogenic heat and their impacts on air quality in South China. *Atmospheric Chemistry and Physics*, 16(23):15011–15031, 2016. doi:10.5194/acp-16-15011-2016.

[27] W. Yang, Y. Luan, X. Liu, X. Yu, L. Miao, and X. Cui. A new global anthropogenic heat estimation based on high-resolution nighttime light data. *Scientific Data*, 4(170116), 2017. doi:10.1038/sdata.2017.116.

[28] P. Forster, V. Ramaswamy, P. Artaxo, T. Berntsen, T. Betts, D. W. Fahey, J. Haywood, J. Lean, D. C. Lowe, G. Myhre, J. Nganga, R. Prinn, G. Raga, M. Schulz, and R. Van Dorland. Changes in Atmospheric Constituents and in Radiative Forcing. In S. Solomon, D. Qin, M. Manning, Z. Chen, M. Marquis, K. B. Averyt, M. M. B. Tignor, and H. L. Jr. Miller, editors, *Climate Change 2007: The Physical Science Basis. Contribution of Working Group I to the Fourth Assessment Report of the Intergovernmental Panel on Climate Change*, pages 129–234. Cambridge University Press, Cambridge, United Kingdom and New York, NY, USA, 2007. URL: https://www.ipcc.ch/site/assets/uploads/2018/02/ar4-wg1-chapter2-1.pdf.

[29] B. Chen, C. Wu, X. Song, Y. Zheng, M. Lu, H. Yang, X. Wu, X. Zhao, Z. Lu, T. Luo, and X. Liu. Anthropogenic heat release due to energy consumption exacerbates European summer extreme high temperature. *Climate Dynamics*, 61(7):3831–3843, 2023. doi:10.1007/s00382-023-06775-x.

[30] X. Song, X. Wu, B. Chen, C. Wu, T. Luo, X. Liu, and G. Shi. Anthropogenic heat release, a non-negligible climatic factor for Eastern China in boreal summer. *Theoretical and Applied Climatology*, 155:5849–5858, 2024. doi:10.1007/s00704-024-04982-y.

[31] B. Chen, C. Wu, X. Liu, L. Chen, J. Wu, H. Yang, T. Luo, X. Wu, Y. Jiang, L. Jiang, H. Y. Brown, Z. Lu, W. Fan, G. Lin, B. Sun, and M. Wu. Seasonal climatic effects and feedbacks of anthropogenic heat release due to global energy consumption with CAM5. *Climate Dynamics*, 52:6377–6390, 2019. doi:10.1007/s00382-018-4528-1.

[32] X. Wang, K. Hu, Y. Hao, Y. Yin, J. Xu, Y. Li, F. Chen, B. Chen, L. Chen, Q. Li, Q. Liu, H. Cai, Y. Liang, P. Wang, and S. Liang. Volatile organic compounds (vocs) emission interferes with real-time regulatory monitoring of ozone in urban atmosphere. *Urban Climate*, 55, May 2024. doi:10.1016/j.uclim.2024.101938.

[33] S. Szopa, V. Naik, B. Adhikary, P. Artaxo, T. Berntsen, W. D. Collins, S. Fuzzi, L. Gallardo, A. Kiendler-Scharr, Z. Klimont, H. Liao, N. Unger, and P. Zanis. Short-Lived Climate Forcers. In V. Masson-Delmotte, P. Zhai, A. Pirani, S. L. Connors, C. Péan, S. Berger, N. Caud, Y. Chen, L. Goldfarb, M. I. Gomis, M. Huang, K. Leitzell, E. Lonnoy, J. B. R. Matthews, T. K. Maycock, T. Waterfield, O. Yelekçi, R. Yu, and B. Zhou, editors, *Climate Change 2021: The Physical Science Basis. Contribution of Working Group I to the Sixth Assessment Report of the Intergovernmental Panel on Climate Change*, pages 817–922. Cambridge University Press, Cambridge, United Kingdom and New York, NY, USA, 2021. URL: https://www.ipcc.ch/report/ar6/wg1/chapter/chapter-6/, doi:10.1017/9781009157896.008.

[34] Our World in Data. Global Plastics Production, 2025. Dataset retrieved March 21, 2026. URL: https://ourworldindata.org/grapher/global-plastics-production.

[35] H. Huang, Z. Wang, C. Dai, J. Guo, and X. Zhang. Volatile organic compounds emission in the rubber products manufacturing processes. *Environmental Research*, 212, part C, September 2022. doi:10.1016/j.envres.2022.113485.

[36] K.-H. Lin, J.-H. Tsai, C.-C. Cheng, and H.-L. Chiang. Emission of volatile organic compounds from consumer products. *Aerosol and Air Quality Research*, 22(9), September 2022. doi:10.4209/aaqr.220250.

[37] K. Qiu, L. Yang, J. Lin, P. Wang, Y. Yang, D. Ye, and L. Wang. Historical industrial emissions of non-methanevolatile organic compounds in china for the period of 1980–2010. *Atmospheric Environment*, 86:102–112, April 2014. doi:10.1016/j.atmosenv.2013.12.026.

[38] M. Li, Q. Zhang, B. Zheng, D. Tong, Y. Lei, F. Liu, C. Hong, S. Kang, L. Yan, Y. Zhang, Y. Bo, H. Su, Y. Cheng, and K. He. Persistent growth of anthropogenic non-methane volatile organic compound (nmvoc) emissions in china during 1990–2017: drivers, speciation and ozone formation potential. *Atmos. Chem. Phys.*, 19:8897–8913, 2019. doi:10.5194/acp-19-8897-2019.

[39] K. K. Tung and C. D. Camp. Solar cycle warming at the Earth's surface in NCEP and ERA-40 data: A linear discriminant analysis. *Journal of Geophysical Research: Atmospheres*, 113(D5):D05114, 2008. doi:10.1029/2007JD009164.

[40] T. Amdur, A. R. Stine, and P. Huybers. Global Surface Temperature Response to 11-Yr Solar Cycle Forcing Consistent with General Circulation Model Results. *Journal of Climate*, 34(8):2893–2903, 2021. doi:10.1175/JCLI-D-20-0312.1.

[41] L.-F. Li and K. K. Tung. Solar cycle as a distinct line of evidence constraining Earth's transient climate response. *Nature Communications*, 14(1):8430, 2023. doi:10.1038/s41467-023-43583-7.

[42] Royal Meteorological Institute of Belgium (KMI). Yearly average temperature in Brussels, Ukkel from 1833 to 2024, 2025. URL: https://www.meteo.be/nl/klimaat/klimaatverandering-in-belgie/klimaattrends-in-ukkel/luchttemperatuur/gemiddelde/jaarlijks.

[43] European Environment Agency. Emissions of ozone precursors, 2025. URL: https://www.eea.europa.eu/en/european-zero-pollution-dashboards/indicators/emissions-of-ozone-precursors-nox-nmvocs-and-methane-indicator.

[44] Polar Science Center, Applied Physics Laboratory, University of Washington. PIOMAS Arctic Sea Ice Volume Reanalysis, 2025. URL: https://psc.apl.uw.edu/research/projects/arctic-sea-ice-volume-anomaly/.

[45] C. D. Jones, J. E. Hickman, S. T. Rumbold, J. Walton, R. D. Lamboll, R. B. Skeie, S. Fiedler, P. M. Forster, J. Rogelj, M. Abe, M. Botzet, K. Calvin, C. Cassou, J. N. S. Cole, P. Davini, M. Deushi, M. Dix, J. C. Fyfe, N. P. Gillett, T. Ilyina, M. Kawamiya, M. Kelley, S. Kharin, T. Koshiro, H. Li, C. Mackallah, W. A. Müller, P. Nabat, T. van Noije, P. Nolan, T. Ohgaito, D. Olivié, N. Oshima, J. Parodi, T. J. Reerink, L. Ren, A. Romanou, R. Séférian, Y. Tang, C. Timmreck, J. Tjiputra, E. Tourigny, K. Tsigaridis, H. Wang, M. Wu, K. Wyser, S. Yang, Y. Yang, and T. Ziehn. The climate response to emissions reductions due to covid-19: Initial results from covidmip. *Geophysical Research Letters*, 48(8), 2021. doi:10.1029/2020GL091883.

# A Summary: first-order LTI-model for troposphere warming

The troposphere is modeled as a set of independent LTI Z-boxes of a thermal capacitor in parallel with a thermal resistor for the different regions (VoI) modeled, as shown in Figure 2. Table [2] gives an overview of the parameters of the first-order model. The relationship between thermal resistances is given by Equation (23). The SAT-warming model is given by Equation (22):

$$\Delta XSAT_r(t) = r_r \cdot [XIRTA_r(t) + XAHR_r(t) + XSITA_r(t)]$$

with $XIRTA_r(t) = IRTA(t)$ the globally uniform anthropogenic warming of the troposphere by increasing net IR-radiation absorption related to $CO_2$-dominated GHG-emissions expressed by Equation (33)

$$IRTA(t) = IRTA(2025) \cdot a_{\mathrm{GHG}}^{(t-2025)} \ \mathrm{mW/m^2}$$

and $IRTA(2025)$ given in table [2]. The contribution of Anthropogenic Heat Release $XAHR(t)$ is location-dependent and is expressed by Equation (14)

$$XAHR_r(t) = XAHR_r(t_0) a^{(t-t_0)/t_\mathrm{r}}$$

with its parameters listed in Figures 7 and $t_\mathrm{r} = 1$ year. The troposphere heating by the region-dependent increase in solar radiation absorption due to Anthropogenic Chemicals Emissions $XSITA_r(t)$ is expressed by Equation (20)

$$XSITA_r(t) = XSITA_r(t_0) \cdot a_{\mathrm{XSITA}}^{(t-t_0)/t_\mathrm{r}}$$

Figures (14), (18), and (19) provide the model results $XSAT_r(t)$, $IRTA(t)$, $XAHR_r(t_0)$ and $XSITA_r(t_0)$ for $\kappa = 0.19$, $\kappa = 0.21$, and $\kappa = 0.23$ determined in section 4.2.

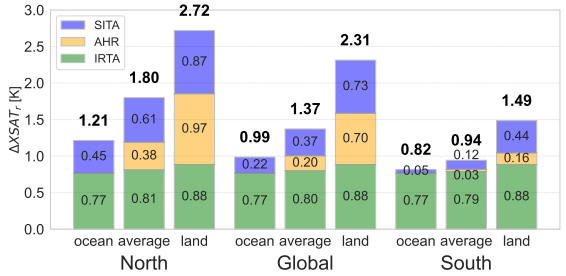


(a) $\Delta XSAT_\mathrm{r}$ contributions in 2025.

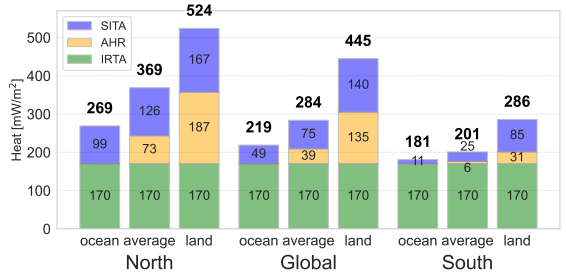


(b) Heat contributions in 2025.

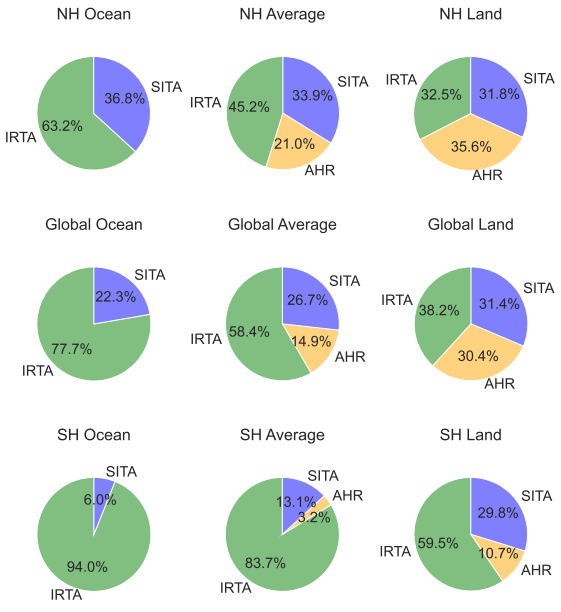


(c) Relative SAT contributions to warming in 2025.

Figure 18: Charts giving the 2025 warming contributions for IRTA, AHR and SITA for different regions based on $\kappa = 0.19 \mathrm{Km^2/W}$ estimate.

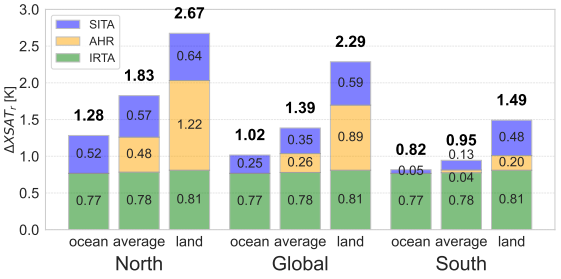


(a) $\Delta XSAT_{\rm r}$ contributions in 2025.

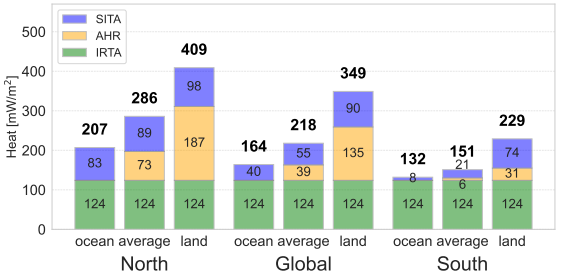


(b) Heat contributions in 2025.

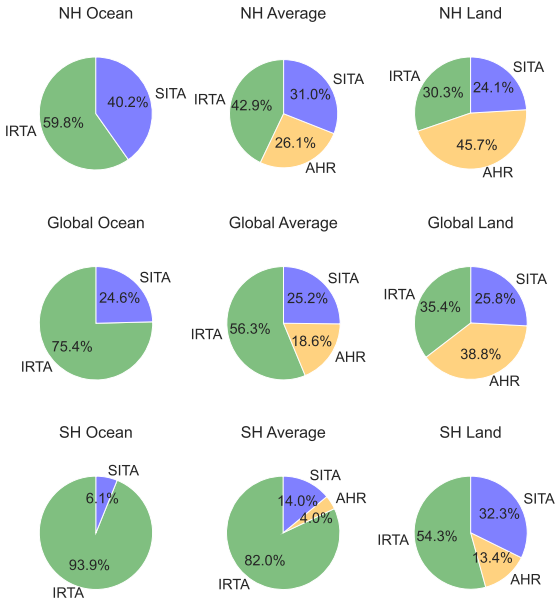


(c) Relative SAT contributions to warming in 2025.

Figure 19: Charts giving the 2025 warming contributions for IRTA, AHR and SITA for different regions based on $\kappa = 0.23 \mathrm{Km}^2/\mathrm{W}$ estimate.

Table 2: Parameters of the troposphere first-order lumped thermal impedance model.NH: Northern Hemisphere. SH: Southern Hemisphere. Uncertainty quantified by two standard deviations except indicated between brackets: the uncertainty on effective thermal resistance over ocean for a given value of $\kappa$ to achieve model consistency.

| Definition | symbol | unit | $\kappa$ [Km$^2$/W] 0.19±0.04 | $\kappa$ [Km$^2$/W] 0.21±0.02 | $\kappa$ [Km$^2$/W] 0.23±0.07 |
|---|---|---|---|---|---|
| Capacity | $c_{\rm t}$ | MJ/Km$^2$ | 7.3 | 7.3 | 7.3 |
| Global impedance | $\lvert z_{\rm G}\rvert$ | Km$^2$/W | 4.0±0.9 | 4.4±0.5 | 5±2 |
| Global resistance | $r_{\rm G}$ | Km$^2$/W | 4.7±0.9 | 5.4±0.9 | 6±2 |
| Relaxation time | $\tau_{\rm G}$ | year | 1.1±0.2 | 1.3±0.2 | 1.5±0.4 |
| Ocean resistance | $r_{\rm ocean}$ | Km$^2$/W | 4.50(±0.05) | 5.25(±0.05) | 6.20(±0.05) |
| Land resistance | $r_{\rm land}$ | Km$^2$/W | 5.2±0.9 | 5.9±0.9 | 7±2 |
| EU resistance | $r_{\rm EU}$ | Km$^2$/W | 2.8±0.5 | 3.1±0.5 | 3±1 |
| Eff. heat source | | | | | |
| IRTA | $IRTA('25)$ | mW/m$^2$ | 170±30 | 150±30 | 120±20 |
| NSITA$_{\rm land}$ | $NSITA_{\rm land}('25)$ | mW/m$^2$ | 170 ± 10 | 120 ± 10 | 100 ± 10 |
| NSITA$_{\rm ocean}$ | $NSITA_{\rm ocean}('25)$ | mW/m$^2$ | 100 ± 10 | 90 ± 10 | 80 ± 10 |
| NSITA growth rate | $\Delta a_{\rm NSITA}$ | %/year | 9.5 ± 0.8 | 11 ± 1 | 12 ± 2 |
| SSITA$_{\rm land}$ | $SSITA_{\rm land}('25)$ | mW/m$^2$ | 85 ± 8 | 74 ± 8 | 74 ± 7 |
| SSITA$_{\rm ocean}$ | $SSITA_{\rm ocean}('25)$ | mW/m$^2$ | 11 ± 5 | 10 ± 4 | 8 ± 4 |
| SSITA growth rate | $\Delta a_{\rm SSITA}$ | %/year | 3.2 ± 0.4 | 3.3 ± 0.5 | 3.2 ± 0.4 |